frontiers | Frontiers in Earth Science

TYPE Original Research
PUBLISHED 26 June 2024
DOI 10.3389/feart.2024.1395384

OPEN ACCESS

EDITED BY
Xixin Wang,
Yangtze University, China

REVIEWED BY
Keji Yang,
Hebei GEO University, China
Sheng Fu,
Xi'an Shiyou University, China

*CORRESPONDENCE
Jia-Peng Liang,
liangjiapeng@mail.cgs.gov.cn

RECEIVED 03 March 2024
ACCEPTED 26 March 2024
PUBLISHED 26 June 2024

CITATION
Dong H-Q, Liang J-P, Zhang Q-Y, Li J-R, Wan J-W, Nie G-Q and Li Y-L (2024), The differential collapse–filling evolution process of the paleo-underground river in the Northern Uplift of the Tarim Basin. *Front. Earth Sci.* 12:1395384. doi: 10.3389/feart.2024.1395384

The differential collapse–filling evolution process of the paleo-underground river in the Northern Uplift of the Tarim Basin

Hong-Qi Dong[1,2], Jia-Peng Liang[2]*, Qing-Yu Zhang[2], Jing-Rui Li[2], Jun-Wei Wan[1], Guo-Quan Nie[2] and Yu-Lu Li[1]

[1]School of Environmental Studies, China University of Geosciences, Wuhan, China, [2]Institute of Karst Geology, Chinese Academy of Geological Sciences/Karst Dynamics Laboratory, MLR and GZAR, Guilin, China

The characteristics and stages of collapse–filling in paleo-underground rivers vary in recharge–runoff–discharge zones, constraining the associated fracture-caved reservoirs in carbonate strata. This paper comprehensively uses core, fluid inclusion, and carbon–oxygen isotope to probe the evolution process and migration of collapse–filling in paleo-underground rivers in the Northern Uplift of the Tarim Basin. The results show that 1) more than three stages of collapse–filling were identified in recharge–runoff–discharge zones, and a four-stage differential collapse–filling process was proposed to summarize the evolution of paleo-underground rivers. 2) The collapse–filling process varies spatiotemporally in the recharge, runoff, and discharge zones. Hydrodynamic strength and filling capacity migrate gradually from the recharge zone to the discharge zone. 3) Collapse–filling mechanisms, including gravity, suffusion, and suction–erosion mechanisms, also vary along with the collapse–filling evolution process of paleo-underground rivers. The research provided a new insight to recognize and interpret the differential planar distribution and vertical filling of the paleo-underground river system, which can be further applied to investigate the fracture-caved karst reservoirs.

KEYWORDS

collapse–filling evolution, paleo-underground river, mechanism, Ordovician carbonate rock, Tarim Basin

1 Introduction

Carbonate rocks can form pores, caves, and fractures at different scales under karstification, which are important storage spaces for oil, natural gas, groundwater, and other resources (James et al., 1988; Yuan, 1993). After multi-stage karstification and continuous transformation, the paleo-underground river became one of the important reservoir spaces that commonly existed in the karst system. However, this reservoir is easily neglected due to its difficulty and complexity in identifying and defining its architecture underground (Loucks et al., 2004; Zhang et al., 2018; Zhang et al., 2020; Zhang et al., 2021; Dan et al., 2023;

Wang et al., 2023; Zhang et al., 2023). During the evolution process of paleo-underground river channel formation and the subsequent multi-stage karst reconstruction, the collapse–filling phenomenon could be clearly observed. Generally, a large number of chemical precipitation, water flow transportation, collapse deposition, and organisms consist of the fillings under physical and chemical interaction (Chen et al., 2023). These fillings change the original reservoir space and can be taken as excellent samples for studying the karst reservoir architecture, evolution process, and formation mechanism (Shi et al., 2015).

Fracture-cave fillings are significant samples for studying the collapse–filling process and further probing karst reservoir formation and transformation process (Liu et al., 2009; Dan et al., 2012; Sun et al., 2013; Qiang et al., 2015). Geochemical analysis of fillings is the common method used to distinguish karst stages, such as the analysis of trace elements in sand–mud filling (Liu and Cai, 2009), isotopic analysis of cave macrocrystalline calcite (Liu et al., 2008), strontium isotope (Zhang et al., 2005; Liu et al., 2006; Liu et al., 2007; Zhang and Cai, 2007), carbon and oxygen isotopes (Winter and Knauth, 1992; Chen, 1994; Wang and Al-Aasm, 2002; Xia and Tang, 2004; Xia et al., 2006; Qian et al., 2008; Ainsaar et al., 2010; Wu et al., 2010; Li et al., 2011; Meng et al., 2011; Xia et al., 2011; Haeri-Ardakani et al., 2013), aqueous inclusion homogenization temperature (Xia and Tang, 2004; Xia et al., 2006; Wu et al., 2010; Xia et al., 2011; Li et al., 2012; Li et al., 2013), and autogenous illite K–Ar dating (Xu et al., 2012). Combined with the analysis of regional tectonic evolution and associated quantitative parameters (Xu et al., 2012; Zhang, 2020), a comprehensive application of a variety of geochemical methods (Zhang et al., 2012; Wang et al., 2017; Lyu et al., 2020) was also used to distinguish collapse–filling stages. However, there is still a lack of suitable methods to classify karst stages in detail by integrating core, isotope, and other means. Moreover, detailed research studies on dissecting karst stages and evolutionary differences of different zones in a unified karst system are rare.

The karst products are characterized by complicated mechanisms and architecture that are difficult to precisely identify underground. More than 70% of the reservoir space of large karst caves is filled with sedimentary mud, sand, collapse breccia, and other materials, which are controlled by complicated filling mechanisms and influencing factors (Xu et al., 2010; Zou et al., 2016; Xu et al., 2020). Loucks et al. (2004) proposed the evolutionary history model of a single karst cave and the collapse model of combined caves and believed that karst caves developed from the near-surface subsurface flow zone were then transformed in the seepage zone, and finally underwent multiple stages and effects such as mechanical compaction and gravity collapse to form karst caves during burial. Studies on many sedimentary basins have proven that the development of paleo-karst was influenced by many factors, such as tectonic movement, weathering and denudation, and burial (Kang et al., 2014). In different stages and zones during the karst evolution process, it is worth considering whether the factors and formation mechanism changed temporally and spatially along with the karst evolution process (Li et al., 2021).

In the northern Tarim Basin, a large paleo-karst cave system was well observed in the mid-Ordovician carbonate rocks under the seismic attributes, and the paleo-underground river channels were widely identified in the karst system (Zhang et al., 2020; Hu, 2022; Lyu et al., 2022). Many scholars explored and analyzed the identification (Zhang et al., 2012), architecture type (Xu et al., 2010; Liu et al., 2021), filling type and distribution rule, filling stage, formation mechanism, reservoir architecture, and prediction of karst caves in the Tahe area (Zou et al., 2016; Sun et al., 2017; Zhang et al., 2017; Xu et al., 2020), but they did not take the formation and evolution of karst caves as a complete karst system to explore the internal relations and differences. Therefore, the fillings of paleo-underground rivers in the weathering crust karst area of the Tahe oilfield were taken as samples in this paper. Based on the observation and description of drilling cores, carbon and oxygen isotope tests, inclusion analysis, logging data analysis, and seismic data interpretation, we depict the filling architecture, analyze the stages of collapse–filling, and discuss the differential evolution process and associated filling mechanism of typical paleo-underground rivers.

2 Geological setting

The Tarim Basin covers an area of 560,000 km^2, and it is the largest oil- and gas-bearing basin in China; it is located between the northern Tianshan Mountain and the southern Kunlun–Altun Mountains (Figure 1A; Jia, 1997). The basin contains the Late Neoproterozoic–Quaternary sediments covering Archean–Early Neoproterozoic crystalline basement with a thickness of more than 10 km (Figure 1B; Wu et al., 2010). The study area is located on the southern slope of the Northern Uplift of the Tarim Basin.

The Ordovician strata in the study area can be divided into the Penglaiba (O_1p), Yingshan (O_1y), Yijianfang (O_2y), Chalbac (O_3q), Lianglitage (O_3l), and Sangtamu (O_3s) formations from the bottom to top. The Middle–Lower Ordovician strata in the area are composed of a set of carbonate rocks formed in the platform facies. The Yingshan Formation is widely distributed in the area and is one of the main formations where karst is widely observed in the study area. The lithology is mainly gray, light gray, and brown–gray thick-bedded micrite, along with algal clot pelletic micrite containing algal sand and gravel calcarenite, and the lithology is dense and easy to dissolve. The strata, therefore, provide a good material foundation for later karstification and associated karst reservoir, which has been proven as a high-quality karst reservoir in the Tahe oilfield (Qi and Yun, 2010; Zhang et al., 2012; Hu et al., 2014; Kang, 2014).

The study area has undergone multiple stages of uplift and associated karstification, and the fracture-cave filling of Ordovician carbonate rocks is characterized by multiple stages and styles (Jin et al., 2015). Specifically, the Ordovician carbonate rocks in this area commonly experienced four stages of exposure and weathering karst processes (Yu et al., 2011; Chen et al., 2016). 1) After the period of the Yijianfang Formation, the study area was uplifted and denudated, with strong weathering and karstification. 2) After the period of the Lianglitage Formation, the study area was exposed again, with the characteristic of structural high in the north and low in the south. 3) Before the Silurian period, some strata were denuded, and several formations such as Yijianfang and Yingshan formations were directly exposed to the surface, forming a pre-Silurian buried hill. 4) In the early Hercynian period, the orogenic belt was strongly folded, and a local unconformity

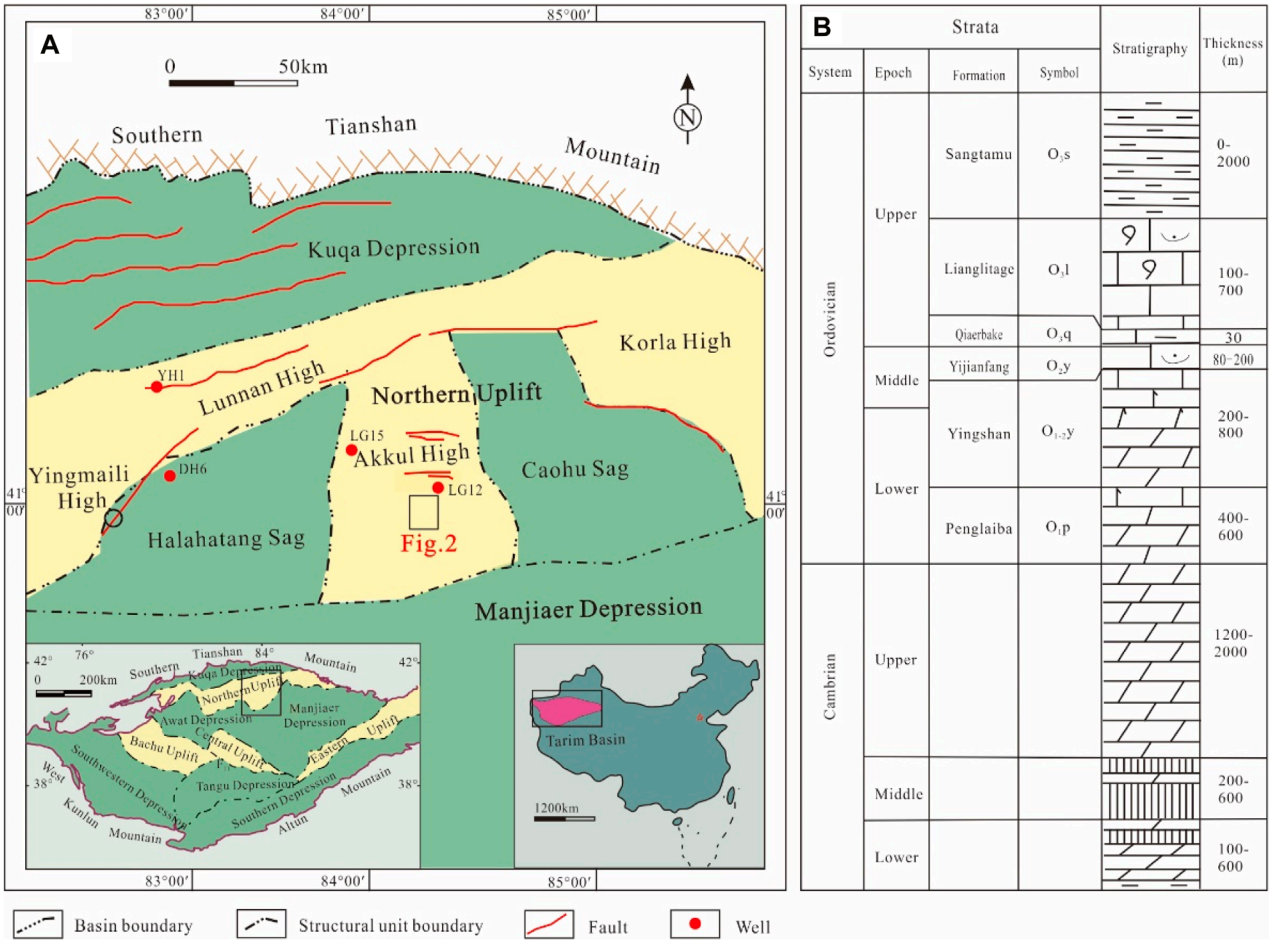

FIGURE 1
Simplified map of the tectonic units **(A)** and comprehensive stratigraphic column **(B)** in the northern Tarim Basin.

between the Middle–Lower Ordovician and the overlying strata was formed.

After multi-stage dissolution and transformation, a series of highly heterogeneous karst reservoir spaces such as paleo-underground rivers, large karst caves, and dissolution caves have been formed in the Yijianfang and Yingshan formations (Xia et al., 2011; Lyu et al., 2020). In the study area, the thickness of affected strata of buried hill karst ranges up to 200 m, and a large-scale karst cave system is formed. The karst cave fillings contain mud, carbonate breccia, and some chemical deposits such as peat and stalactites. During the reconstruction process of dissolution, collapse, and filling, the structural characteristics in different parts of the paleo-underground river are quite different (Zhang, 1985; Liu and Cai, 2009).

3 Data and methodology

3.1 Methodology for karst cave architecture analysis

A solutional cave is a macroscopic void in a rock created and shaped by moving aggressive fluids, and morphology is the fundamental attribute of the cave that reflects its origin and evolution. Thus, morphogenetic analysis of the caves aims to reconstruct the geological controls of the speleogenesis and parameters of speleogenetic agents (fluids) (Klimchouk et al., 2016). Important attributes of fluids that determine various aspects of cave morphology are their aggregate states and various modes of movement and aggressiveness (Lauritzen and Lundberg, 2000). These attributes differ between various hydrodynamic zones, types of flow systems, and components of the latter. The relationships between morphologic features (also termed forms, speleomorphs, and speleogens) and speleogenetic agents were established, although not always unequivocally, from generalizations based on field observations and physical and numerical models (Bögli, 1980; Ford and Williams, 1989; Lauritzen and Lundberg, 2000; Palmer, 2007; Klimchouk et al., 2016).

Figure 2 was mapped using the above methodology. The RMS amplitude space ranging from 40 to 120 ms (confidential data) under the bottom of the Middle Ordovician Yijianfang Formation and paleo-topography after the period of the Middle–Lower Ordovician Yingshan Formation was comprehensively applied to constrain and describe the paleo-channels in the Yingshan Formation.

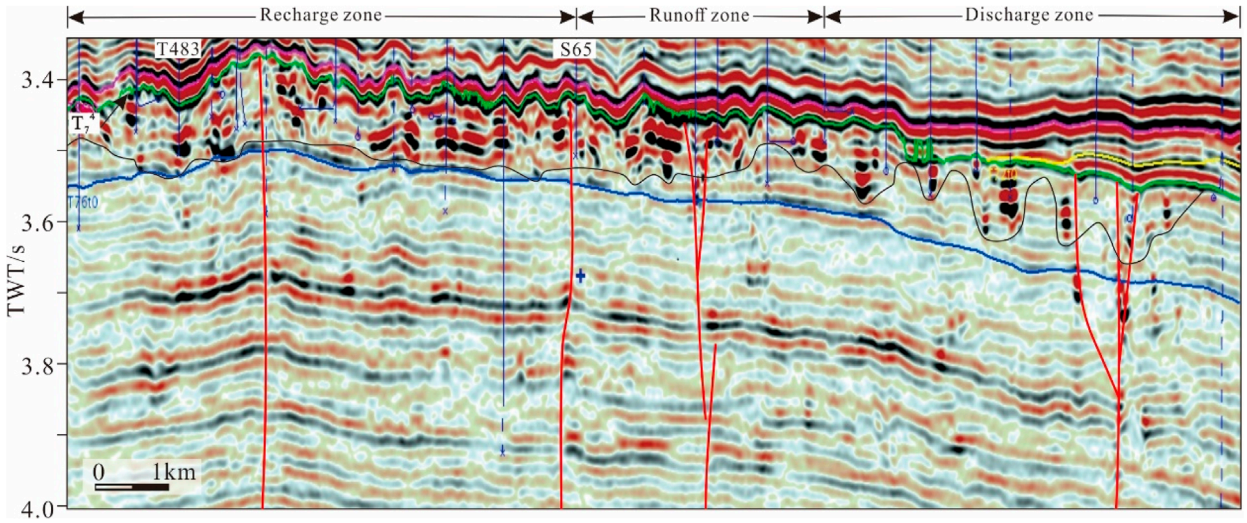

FIGURE 2
Typical paleo-underground river channel on the seismic profile (T_7^4, top of Yijianfang Formation; the profile location is shown as a red line in Figure 3; the red line denotes fault, the black line denotes the bottom boundary, and the blue line denotes the well.).

3.2 Geochemical method for cave filling analysis

3.2.1 Carbon and oxygen isotopes

All of the 22 samples were collected in the paleo-underground river in the Yingshan Formation in the Upper–Middle Ordovician strata. The collected samples were subjected to grinding, drying, acidification, and other pretreatments, and then tested for carbon and oxygen isotope composition. The test work was completed by the Karst Geological Resources and Environmental Supervision and Inspection Center of the Ministry of Nature Resources. A stable isotope mass spectrometer (Item no.: MAT253, Thermo Fisher Scientific, Waltham, MA, American) was used to test $\delta^{13}C$ and $\delta^{18}O$. The test precision was 0.1‰. The ambient temperature and relative humidity were 24.3°C and 40%, respectively.

3.2.2 Fluid inclusion of calcite

All samples were calcite in fracture caves from one underground river system developed in the Yingshan Formation in the Upper–Middle Ordovician strata. The homogenization temperature (Th) and ice temperature (Tm) data involved were completed at the Karst Geological Resources Environmental Monitoring Center, Ministry of Natural Resources. The instrument used was a Linkam hot and cold table, model THMS600. The salinity (wt% NaCl equivalent) of aqueous inclusions was calculated based on Tm values.

4 Results

4.1 Distribution and architecture of the paleo-underground river

The study area mainly shows the structural characteristics that north is higher than south, which belongs to the karst platform-peak cluster depression landform in the karst geomorphology, and the more detailed division belongs to the karst gentle slope land-peak cluster ridge valley landform (Figure 3). Through the interpretation of the paleo-geomorphological map, it was found that the surface and underground river channels in the study area were obviously developed, the surface and underground river channels in the study area were further characterized, and the development characteristics of the channels were defined, in addition to the transformation positions of the surface and underground river. The surface runoff was mainly in the NE and NW directions, which is consistent with the development direction of strike–slip faults, but some transverse river systems also developed, which were related to the local geomorphology. From north to south, surface runoff gradually converged southward from each tributary into the karst lake. Surface runoff entered the underground river system mainly through depressions, sinkholes, and voltamps. In the whole study area, the development of the underground river channels had obvious zonal characteristics. With well T416 as the boundary, the underground river channels mainly developed in the NNW direction in the east, while the underground river channels differed from north to south in the west, which showed that the channels mainly developed in the NNW direction and nearly in the EW direction in the north, and the overall trend changes to the NE direction, which is more consistent with the development position of the NE direction fault in the south.

On the seismic profile, the top Yingshan Formation gradually decreased from north to south, with the paleo-underground channels characterized by strong amplitude within the Yingshan Formation, which could be identified using seismic data. However, from north to south, there were significant differences observed in the seismic characteristics of the paleo-underground channels in the recharge–runoff–discharge zones. In the recharge zone, the paleo-underground channel mainly was characterized by weak-to-moderate continuity seismic reflection events, locally strong amplitude, and more chaotic reflections on the seismic

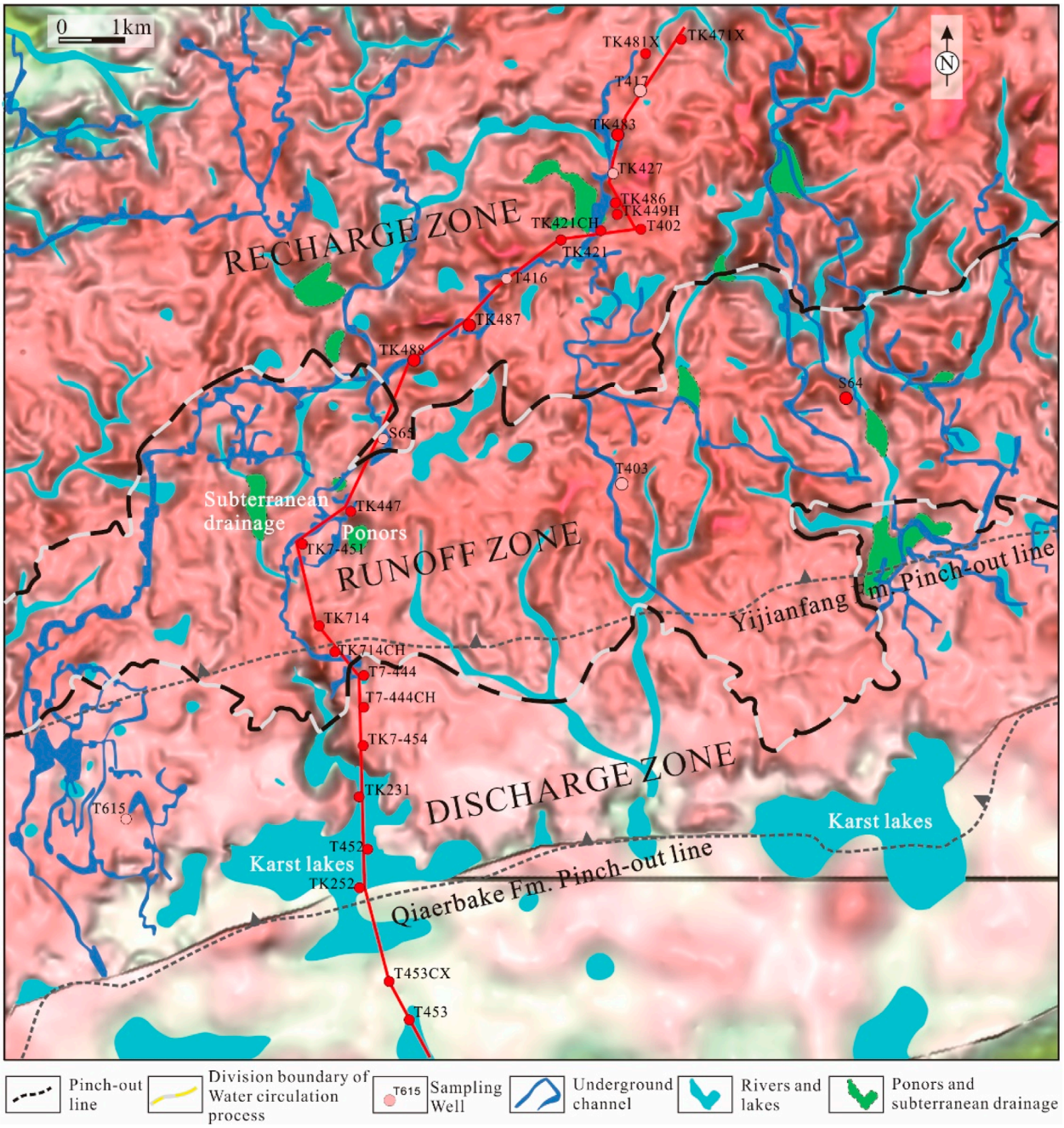

FIGURE 3
Paleo-karst topography of the paleo-underground river in the Tahe oilfield.

profile. In the runoff area, paleo-underground channels mainly exhibited strong continuity seismic reflection events, with strong amplitude in continuous sections and local scattered reflections. In the discharge area, the overall characteristics of the paleo-underground channel showed weakened amplitude and limited scale, but seismic reflection events were relatively continuous. Strong amplitude reflection could be only observed at a certain depth in local areas. The strong amplitude reflection area was discontinuous and appeared as "beading" vertically.

4.2 Multiphase collapse–filling architecture of the paleo-underground river

The paleo-underground channels showed significant seismic geological differences in different recharge–runoff–discharge zones in a whole karst water system, including the recharge, runoff, and discharge zones. This study selected and probed three typical wells in different karst areas to analyze the architecture of the paleo-underground channels, with a focus on dissecting the collapse–filling architecture.

4.2.1 Paleo-underground river channel architecture in the recharge zone

The initial part of the paleo-underground channel belonged to the recharge area of the karst water system; the channel ranged from 1 to 22.6 m, and the hall-type karst cave was locally developed. Well TK483 was observed to be a typical well located in the recharge area (Figure 3), belonging to the karst platform-peak cluster and trough valley of karst geomorphology, with depression and sinkhole existing. Well TK483 was located in the conversion area where both surface and underground rivers developed. From the results of core observation (Figure 4), the well entered the Yingshan Formation at 5526.0 m; drilling encountered a karst cave with a height of 19.8 m at the well depth of 5535.0–5554.8 m. A karst cave with a height of 20 m could be observed at the well interval of 5678.0–5698.0 m. Specifically, at the depth of 5665.0–5676.0 m, there was a fractured zone at the top of the cave. The karst body was mainly composed of dissolution fractures and pores, which were partially filled with calcium mud (Figure 4A), resulting in severe drilling losses. Since entering the cave, the resistivity curve shows a downward trend and slightly increases in some areas. The cave appeared to be characterized by a multi-layer filling architecture from top to bottom. The upper part of the cave (5678.0–5682.0 m) was partially filled with calcareous mudstone (Figure 4B), with a porosity greater than 5%. The middle part of the cave (5682.0–5684.0 m) was filled with calcium mud-cemented collapsed breccia, with a porosity greater than 5%. The lower part of the karst cave (5684.0–5686.0 m) was partially filled with calcareous mudstone, with a porosity greater than 5%. The bottom of the karst cave (5686.0–5692.0 m) was fully filled with karst breccia and calcareous mudstone (Figure 4C), with a porosity of 2%–2.5%. The fractured zone at the bottom of the cave (5692.0–5698.0 m) was filled with calcium mud, with a porosity of 2%–2.5%, and a slight decrease in the resistivity curve could be observed in this interval.

4.2.2 Paleo-underground river channel architecture in the runoff zone

Well T403 was located in the runoff area of the karst subsystem (Figure 3), with a channel size of 1.5–20 m. This well was also developed in the west wall of the NW-striking strike–slip fault. There were numerous fractures and fractured rocks observed in this area, and the landform was the karst platform-to-peak cluster depression landform.

Karstification was mainly observed in the Yingshan Formation (Figure 5). Well T403 entered the Yingshan Formation at a depth of 5405.0 m. The depth of 5487.4-5554.4 m was th karst cave, while the depth of 5488.0-5488.8 m, 5503.9-5507.5 m and 5538.9-5542.4 m were developed by dissolution fractures and pores, which were filled with calcium and mud. The resistivity curve sharply decreased from the beginning of the karst section and showed obvious fluctuations. The 5488.0–5488.8 m section was filled with gray–green calcareous mudstone (Figure 5A), and the top dissolution fractures were filled with calcite without breccia. The 5503.9–5507.5 m section was filled with gray–green calcium mud, containing limestone breccia (Figure 5B), which was distributed in a suspended state. The upper part of the 5538.8–5542.6 m section was fully filled with sand and mud (Figure 5C), while the lower part was filled with karst breccia and cemented with mud, sand, and quartz sandstone (Figures 5D,E). The degree of breccia roundness and sorting was observed to be moderate, and the arrangement of the breccia showed the direction of paleo-curbation.

4.2.3 Paleo-underground river channel architecture in the discharge zone

Well T615 was located in the discharge area of the karst subsystem (Figure 3), which belongs to the top of the steep slope of the peak cluster karst hilly depression. Well T615 was located at the edge of the valley, near the development of a sinkhole. The location of the well was found to belong to the outflow section of the underground river, which is the outflow type channel with a size of 2–49 m.

Karstification was mainly observed in the Yingshan Formation (Figure 6). Well T615 entered the Yingshan Formation at a depth of 5520.9 m. The karst cave developed at a depth of 5520.9–5560.0 m, with a height of 39.1 m, and was observed to be located in the runoff zone. The well had the following logging response characteristics at a depth of 5520.9–5560.0 m: the natural gamma value increased abnormally from 10 API to 65 API; the resistivity was abnormally low, as low as 10 Ω; the karst cave was fully filled with sandstone and gray–green calcareous mudstone, with parallel bedding and small–medium cross-bedding. There were three layers of limestone breccia observed at the bottom, middle–upper, and top of the karst cave. The top limestone breccia had the largest volume and poor roundness and sorting, while the bottom limestone breccia had a smaller volume and better roundness and sorting.

At a depth of 5520.9–5527.6 m the top part of the karst cave, near the weathering crust, was observed. The karst development degree was higher, mainly developing high-angle fractures, filled with gray–green calcareous mudstone, and a small amount of breccia with poor rounding and poor sorting (Figure 6A). The well section, at a depth of5533.4–5560.6 m, was composed of arenaceous micrite and cave filling material. The karst cave height was found to be approximately 19 m, and the lithology of the top of the karst cave was mainly light gray arenaceous micrite bedrock, developed high-angle fractures, filled with gray–green calcareous mud and limestone breccia with poor rounding and poor sorting (Figure 6B). The cave was fully filled with fine sandstone and gray–green calcareous mud, with parallel bedding, and small–medium cross-bedding could be seen (Figure 6C). This karst cave was a sandstone reservoir with an oil leaching phenomenon. A series of limestone breccia was developed in the middle–upper part of the karst cave, and the roundness and sorting of the limestone breccia were better than those in the top part. The bottom of the cave was mainly composed of gray micrite and cave fillings, and high-angle fractures were developed (Figure 6D). The fractures were filled with gray–green calcareous mud and breccia with poor sorting and rounding.

4.3 Geochemical characteristics of collapse–fillings of the paleo-underground river

4.3.1 Characteristics of carbon and oxygen isotopes

The carbon and oxygen isotope values of 22 samples were tested (Table 1). $\delta^{13}C$ values in the recharge area ranged from −3.83‰ to

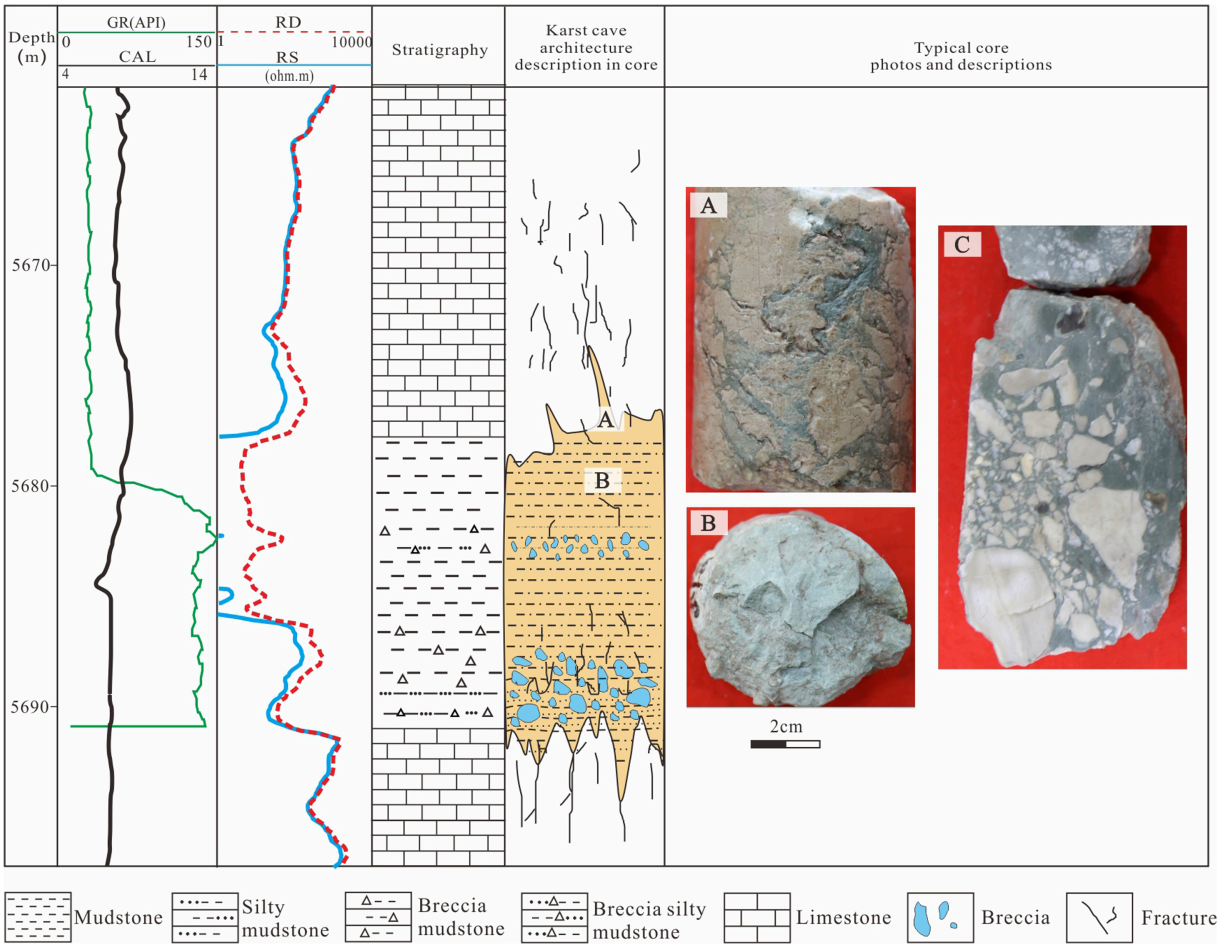

FIGURE 4
Comprehensive column of well T483 illustrating multiphase filling features of the paleo-underground river in the recharge zone (well location is shown in Figure 3). **(A)** mud fillings of fracture in the top of cave; **(B)** mud fillings in the middle of cave; **(C)** argillaceous cement breccia in the bottom of cave.

−0.66‰, with an average value of −1.51‰, and $\delta^{18}O$ values ranged from −12.34‰ to −7.5‰, with an average value of −8.63‰. In the runoff zone, $\delta^{13}C$ values ranged from −4.41‰ to −0.97‰, with an average value of −2.26‰, and $\delta^{18}O$ values ranged from −10.56‰ to −7.11‰, with an average value of −8.8‰. In the discharge zone, $\delta^{13}C$ values ranged from -5.62‰ to −0.12‰, with an average value of −2.94‰, and $\delta^{18}O$ values ranged from −12.43‰ to −7.11‰, with an average value of −9.51‰. The $\delta^{13}C$ and $\delta^{18}O$ values of fillings in different zones are different, reflecting the filling characteristics in different filling environments.

According to the carbon–oxygen isotope intersection chart (Figure 7), the filling stages were divided into the following four stages: in the first stage, the $\delta^{13}C$ values ranged from −4.72‰ to −0.12‰, and the $\delta^{18}O$ values ranged from −10.86‰ to −7.11‰. In the second stage, the $\delta^{13}C$ values ranged from −3.83‰ to −3.07‰, and the $\delta^{18}O$ values ranged from −12.43‰ to −12.34‰. In the third stage, the $\delta^{13}C$ values ranged from −4.41‰ to −2.45‰, and the $\delta^{18}O$ values ranged from −10.81‰ to −9.14‰. The $\delta^{13}C$ and $\delta^{18}O$ values of the fourth phase are 5.62‰ and −8.14‰, respectively.

4.3.2 Characteristics of fluid inclusion

A total of 203 gas–liquid two-phase fluid inclusions were tested using fractured-cave calcite samples obtained from four typical wells (T417, T403, S65, and T615) for inclusion homogenization temperature and ice temperature tests (Table 2). The results showed that the inclusions were mainly distributed in zonation and cluster distribution (Figure 8). The lowest homogenization temperature was 78°C and the highest was 155°C, and no low-temperature inclusions below 70°C were detected. Some calcite contained single-liquid phase inclusions, and calcite inclusions were formed at low temperatures in the reaction. From the homogenization temperature distribution histogram of inclusions (Figure 9A), it could be seen that fluid inclusions were mainly distributed in two temperature segments of 85°C–100°C and 115°C–130°C.

In the recharge zone, taking well T417 as an example, 90 saline inclusions were statistically analyzed, and the inclusions were mainly distributed in zonation, elliptical and rectangular in shape, with sizes ranging from 2 μm to 20 μm, and homogenization temperature ranging from 78°C to 134°C. There were at least two peaks in the frequency histogram (Figure 9B), with 45 inclusions with the highest

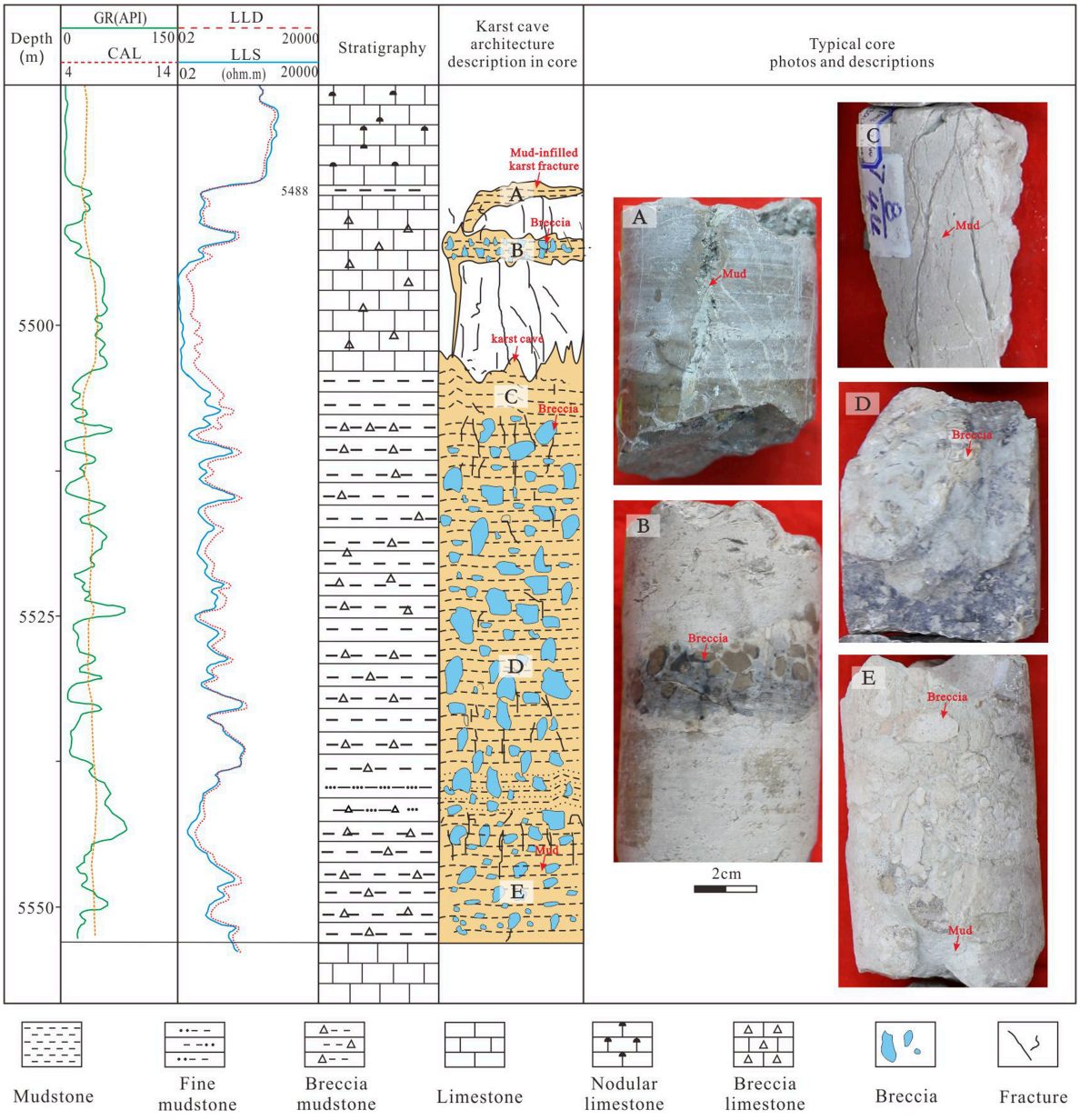

FIGURE 5
Comprehensive column of well T403 illustrating filling features of the paleo-underground river in the runoff zone (well location is shown in Figure 3). **(A)** mud fillings of fracture in the top of cave; **(B)** argillaceous cement brecciain of the fracture in the top of cave; **(C)** mud fillings in the top of cave; **(D)** argillaceous cement big breccia in the middle of cave; **(E)** argillaceous cement small breccia in the bottom of cave.

frequency ranging from 85°C to 100°C, followed by 19 inclusions at 115°C–130°C.

In the runoff zone, 37 inclusions from well T403 and 60 inclusions from well S65 were analyzed, respectively. The inclusions of well T403 were distributed in zonation and free form, and the morphology was mainly rectangular and polygonal, followed by diamond shapes, nearly oval shapes, and a small number of irregular shapes. The size of inclusions was observed to be between 3 and 35 μm, and the homogenization temperature was between 95°C and 155°C. In the frequency histogram (Figure 9C), there were at least two peaks, with the highest frequency in the temperature range of 130°C–145°C, with up to 11 inclusions, and the second in the temperature range of 145°C–160°C, with 10 inclusions. The inclusions were mainly distributed in free and small zonation, with rectangular followed by oval shapes. The size of inclusions ranged from 3 to 30 μm. The homogenization temperature span between 80°C and 140°C in the frequency histogram (Figure 9D) between 85°C and 100°C, and there were 36 samples in total.

In the discharge zone, taking well T615 as an example, the inclusions were mainly distributed in zonation, followed by clusters,

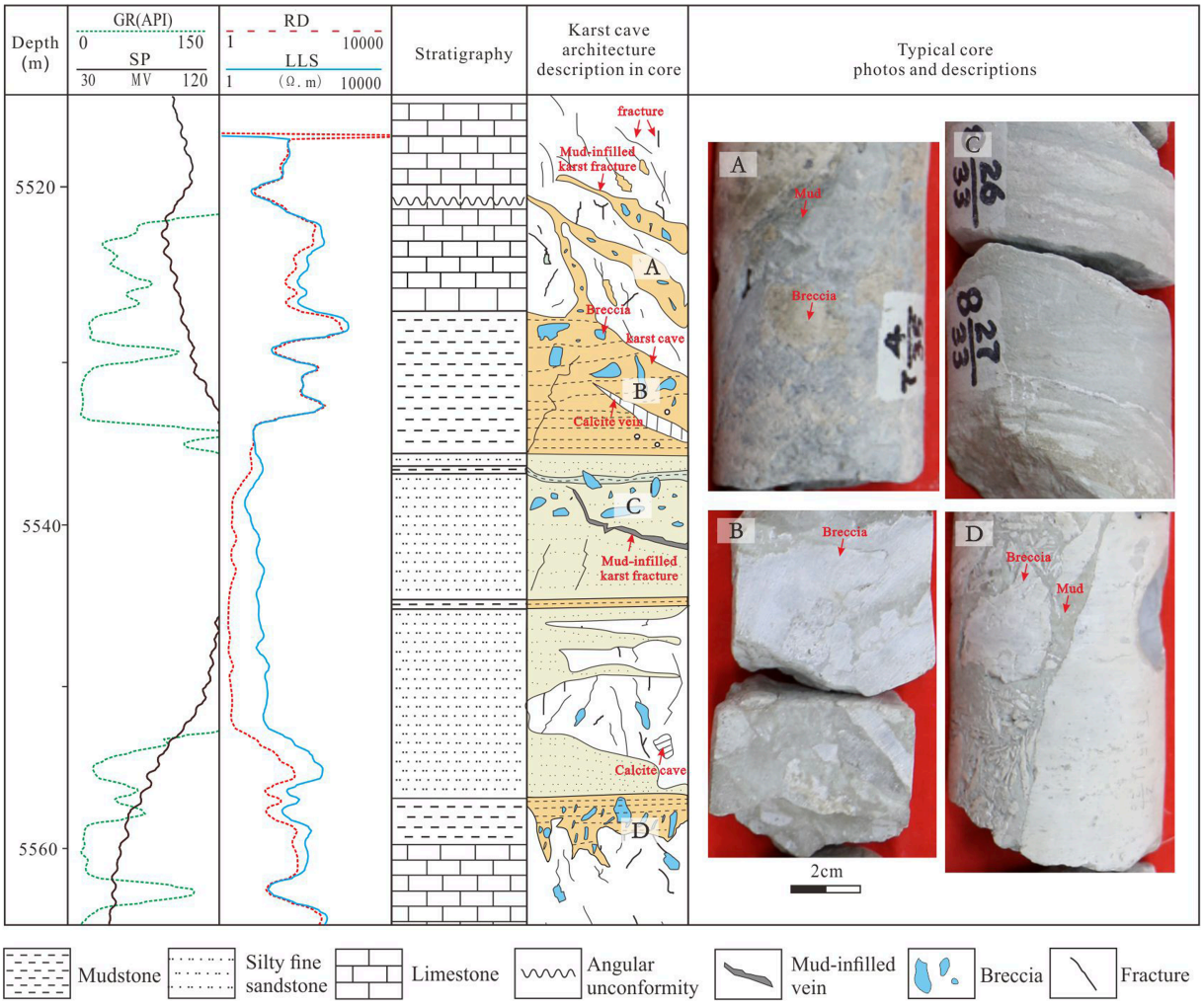

FIGURE 6
Comprehensive column of well T615 illustrating filling features of the paleo-underground river in the discharge zone (well location is shown in Figure 3). **(A)** argillaceous cement brecciain of the fracture in the top of cave; **(B)** argillaceous cement brecciain in the top of cave; **(C)** sandy fillings in the top of cave; **(D)**. argillaceous cement big breccia in the middle of cave.

with irregular shapes and oval shapes. The size of inclusions ranged from 3 μm to 74 μm, the homogenization temperature span ranged from 80°C to 107°C, and there was a peak of eight inclusions ranging from 85°C to 100°C (Figure 9E).

5 Discussion

5.1 Multiphase collapse–filling process in the paleo-underground river

Generally speaking, the core is one of the most intuitive pieces of evidence for understanding the basic architecture of paleo-underground channels. A series of test analyses based on core samples can further distinguish the formation environment and filling stage of the paleo-underground channels (Dan et al., 2023; Zhang et al., 2020; Zhang et al., 2021; Zhang et al., 2023; Wang et al., 2023; Zhang et al., 2018; Chen et al., 2023; Shi et al., 2015). Some scholars have analyzed the filling architecture and formation stage of the paleo-underground channels in the Tahe area according to their characteristics (Zhang et al., 2018; Zhang et al., 2020; Zhang et al., 2021; Chen et al., 2023; Zhang et al., 2023), but the differences in filling architecture of different recharge–runoff–discharge zones and the relationship between karst stages have been ignored. In this paper, the core filling characteristics and structural differences of three typical wells in three recharge–runoff–discharge zones were analyzed, and the analysis of fluid inclusion and carbon–oxygen isotope was carried out to comprehensively explore the internal relations and differences between different recharge–runoff–discharge zones, providing hydrogeological basis for the study of the distribution law and development degree of karst reservoirs and providing evidence for the study of karst fracture-cave architecture and filling characteristics of the karst fracture-cave system.

TABLE 1 Test results of $\delta^{13}C$ and $\delta^{18}O$ (PDB standard).

Well	Depth(m)	Lithology	Source	$\delta^{13}C_{(V\text{-}PDB)}$‰	$\delta^{18}O_{(V\text{-}PDB)}$‰
S64	5489.0	Calcareous mud	Calcareous mud-filled caves	−1.35	−9.43
S64	5491.0	Calcium film	Calcium fillings	−1.57	−8.77
T403	5403.0	Calcareous mud	Paleo-weathering crust	−1.12	−7.66
T403	5429.0	Limestone	Bedrock	−0.97	−7.11
T403	5488.6	Calcareous mud	Calcareous mud-filled caves	−4.41	−9.84
T403	5504.0	Calcareous mud	Calcareous mud-filled caves	−3.95	−9.14
T403	5509.0	Calcareous mud	Calcareous mud-filled caves	−2.29	−7.89
T403	5536.8	Calcareous mud	Cave fillings	−2.45	−10.56
T416	5427.0	Breccia	Cave breccia	−1.09	−7.5
T417	5507.0	Calcite	Calcite-filled caves	−3.83	−12.34
T615	5536.0	Micrite	Micrite in the fracture wall	−0.12	−7.75
T615	5521.5	Calcareous mud	Calcareous mud-filled caves	−4.72	−10.86
T615	5521.6	Calcite	Calcite in the fracture wall	−5.62	−8.14
T615	5534.5	Argillaceous siltstone	Argillaceous siltstone-filled caves	−3.21	−9.46
T615	5552.0	Calcareous mud sandstone	Calcareous mud sandstone-filled caves	−3.07	−12.43
T615	5558.2	Sandstone	Sandstone filled caves	−3.32	−10.81
T615	5558.5	Limestone breccia	Breccia at the bottom of caves	−0.5	−7.11
TK427	5431.0	Limestone breccia	Breccia filled caves	−1.13	−8.26
TK427	5432.4	Limestone	Bedrock at the top of caves	−0.66	−8.27
TK427	5433.0	Limestone	Breccia at the top of caves	−0.75	−7.5
TK427	5434.0	Limestone	Surrounding rock in the middle of caves	−1.52	−8.3
TK427	5435.0	Limestone	Bedrock at the bottom of caves	−1.6	−8.22

5.1.1 Collapse–filling characteristics from core analysis

Through detailed dissections of fracture-cave filling characteristics from the core and results of logging curves, different collapse–filling architectures in different recharge–runoff–discharge zones can be obviously observed, and the collapse–filling stages in different zones are also different.

In the recharge zone, taking well T483 as an example, a karst cave was observed in the well section at a depth of 5678.0–5698.0 m with a height of 20 m. According to the difference in fill lithology and architecture, we believe that at least three stages of collapse–filling process existed in this cave. The first stage was mainly characterized by large karst breccia and calcareous cementation, and the bottom of the karst breccia was covered with mud upward (Figure 4C), which was a combined result of the top collapse and calcareous filling. The calcareous material was the product of accumulation by runoff. During the second stage, smaller karst breccias and calcareous cementation filled above the early fillings. The third stage was characterized by calc-argillaceous cementation in the fractures of the top of the cave, which was the result of seepage filling in the later burial process.

Well T403 is a good example to study the collapse–filling process in the runoff zone. Core data confirmed that a 67-m high karst cave could be observed in the 5487.4–5554.4 m well section, with at least four stages of collapse–filling occurring inside the cave. The most prominent feature during the first stage was the calcium mud-cemented karst cave breccia, located at a depth of 5549.0–5554.4 m, at the bottom of the cave. This is the residual breccia of the underground river formation process, with a particle size relatively small (Figure 5E). The representative products of the second stage

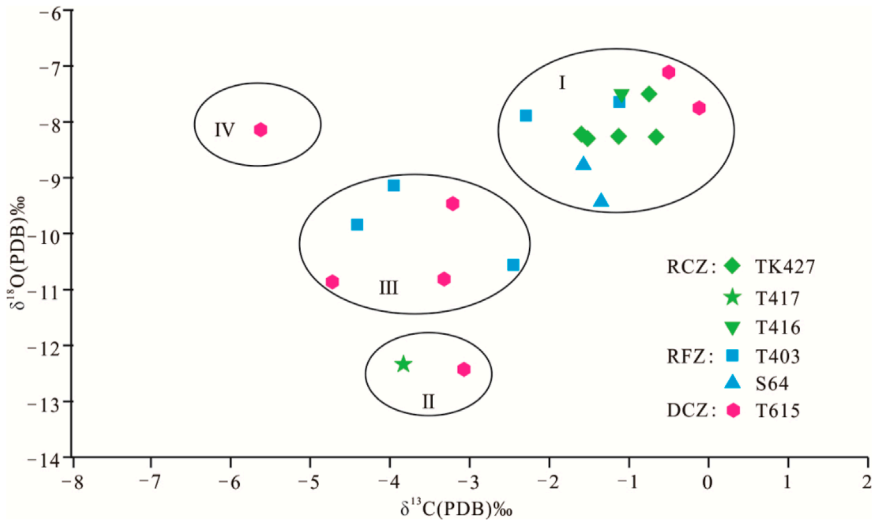

FIGURE 7
Carbon–oxygen isotope crossplot of karst fracture-cave fillings and bedrock (RCZ, recharge zone; RFZ, runoff zone; DCZ, discharge zone).

were karst cave breccia and siltstone cemented by calcium and mud (Figure 5D), where the breccia was larger than in the previous stage. It was formed during the burial process of the underground river and included the collapse materials of the cave ceiling and the runoff sand–mud fillings cemented by calcium. In addition, local bedding could be observed, which was formed during the burial process of the underground river. Thicker sediments were deposited in this stage, and they were probably formed by the superposition of more than one stage of collapse and filling. The third stage was characterized by smaller karst breccias and calcium mud fillings, which filled the branch cavities above the main cave (Figure 5B). During the fourth stage, gray–green and brown calcium mud cement filled above the previous fillings in the cave (Figure 5A), with the filling part belonging to the fracture zone at the top of the cave at a depth of 5487.4–5510.0 m and formed by groundwater infiltration and filling during the burial process.

Well T615 is the example chosen to illustrate the filling features in the discharge area. In this well, a karst cave with a height of 39.1 m was observed. The fillings are characterized by complex lithology and filling style inside the cave and include the karst breccia, sandy mud, calcareous mud, calcite, and other rocks. According to the filling characteristics of the lithological differences, we believe that the karst cave underwent at least five stages of the collapse–filling process. During the first stage, gray micrite filled the karst cave, and high-angle fractures filled with gray–green calcareous clay and breccia also developed (Figure 6D), which may be related to the common strike–slip faults in the study area. During the second stage, sandstone and gray–green calcareous fillings were deposited, with features such as parallel bedding and small–medium-sized cross-bedding, which were products carried by runoff. The argillaceous layer with horizontal bedding filled here may be another stage of filling caused by hydrodynamic or provenance changes. The fillings in the third stage were the mixed collapsed breccia, sand, and mud (Figure 6C). The fillings in the fourth stage were gray–green calcareous clay and a small amount of karst breccia (Figure 6B), and the pores diffused along the fractures in the top of the cave were also filled with calcareous clay and breccia (Figure 6A), which may have been filled at the same time and may have been filled by materials carried by runoff or vertical seepage. In the fifth stage, the fractures in the top cave were filled in, and the calcite veins developed in the well may be the chemical filling formed at a later stage.

5.1.2 Collapse–filling characteristics from geochemical analysis

Three typical wells were selected from three different zones, such as recharge, runoff, and discharge zones, and the filling material in the paleo-underground river channels was sampled, with fluid inclusion and carbon–oxygen isotope tests carried out using these samples. The core characteristics analyzed above confirmed the different characteristics of multi-stage filling in different zones. The filling materials of different rock types were selected for analysis, and their geochemical characteristics were subsequently analyzed. The fluid inclusion temperature measurement results and carbon–oxygen isotopes also suggested that the study area underwent multiphase collapse–filling stages with differential features in different recharge–runoff–discharge zones. It reflected the formation of paleo-karst filling in different karst dynamic systems, which was also supported by other researchers (Cai et al., 2009; Liu and Cai, 2009; Qian et al., 2009; Chen et al., 2023).

In well T417 of the recharge area, three types of fluid inclusions, zonation, small cluster, and free form, can be captured under three different karst dynamic systems. These represent three different karst environments, which may indicate at least three stages of filling processes in the karst cave; however, it was difficult to determine the sequence of formation periods for each type of inclusion. In addition, the formation time of the three types of fluid inclusions may be close and could not be separated by homogenization temperature. Two peaks of homogenization temperature tested from fluid inclusions represent at least two

TABLE 2 Th and distribution characteristics of inclusions in different zones.

Zone	Well	Distribution characteristic	Th (°C)	Well	Distribution Characteristic	Th (°C)
Recharge zone	T417	Zonal distribution	78	T417	Zonal distribution	95
	T417	Zonal distribution	82	T417	Zonal distribution	95
	T417	Zonal distribution	84	T417	Zonal distribution	95
	T417	Zonal distribution	85	T417	Zonal distribution	95
	T417	Free-form distribution	85	T417	Zonal distribution	95
	T417	Free-form distribution	85	T417	Zonal distribution	95
	T417	Free-form distribution	85	T417	Zonal distribution	95
	T417	Zonal distribution, healing microscopic cracks along calcite	85	T417	Zonal distribution	98
	T417	Zonal distribution, healing microscopic cracks along calcite	85	T417	Zonal distribution	98
	T417	Zonal distribution, healing microscopic cracks along calcite	85	T417	Zonal distribution	101
	T417	Zonal distribution, healing microscopic cracks along calcite	86	T417	Zonal distribution	102
	T417	Zonal distribution, healing microscopic cracks along calcite	87	T417	Zonal distribution	108
	T417	Zonal distribution, healing microscopic cracks along calcite	87	T417	Zonal distribution, healing microscopic cracks along calcite	110
	T417	Zonal distribution	88	T417	Zonal distribution, healing microscopic cracks along calcite	110
	T417	Free-form distribution	89	T417	Zonal distribution, healing microscopic cracks along calcite	110
	T417	Free-form distribution	89	T417	Zonal distribution	112
	T417	Free-form distribution	89	T417	Zonal distribution	112
	T417	Free-form distribution	89	T417	Zonal distribution	112
	T417	Free-form distribution	89	T417	Zonal distribution	114
	T417	Zonal distribution	90	T417	Zonal distribution	115
	T417	Zonal distribution	90	T417	Zonal distribution	115

(Continued on the following page)

TABLE 2 (*Continued*) Th and distribution characteristics of inclusions in different zones.

Zone	Well	Distribution characteristic	Th (°C)	Well	Distribution Characteristic	Th (°C)
	T417	Zonal distribution	90	T417	Zonal distribution	115
	T417	Zonal distribution	90	T417	Zonal distribution	115
	T417	Zonal distribution	90	T417	Zonal distribution	115
	T417	Zonal distribution	90	T417	Zonal distribution	115
	T417	Zonal distribution	90	T417	Zonal distribution	116
	T417	Zonal distribution	90	T417	Zonal distribution	118
	T417	Zonal distribution	90	T417	Zonal distribution	118
	T417	Zonal distribution	90	T417	Zonal distribution	118
	T417	Zonal distribution	90	T417	Zonal distribution	118
	T417	Zonal distribution	90	T417	Zonal distribution	120
	T417	Zonal distribution	90	T417	Small-cluster distribution	120
	T417	Zonal distribution	90	T417	Small-cluster distribution	120
	T417	Zonal distribution	90	T417	Small-cluster distribution	120
	T417	Zonal distribution	91	T417	Small-cluster distribution	120
	T417	Zonal distribution	91	T417	Small-cluster distribution	120
	T417	Zonal distribution	92	T417	Small-cluster distribution	122
	T417	Zonal distribution	92	T417	Small-cluster distribution	122
	T417	Zonal distribution	92	T417	Small-cluster distribution	125
	T417	Zonal distribution	92	T417	Small-cluster distribution	125
	T417	Zonal distribution	92	T417	Small-cluster distribution	125
	T417	Zonal distribution	92	T417	Zonal distribution	128
	T417	Zonal distribution	92	T417	Zonal distribution	128
	T417	Zonal distribution	92	T417	Zonal distribution	130
	T417	Zonal distribution	95	T417	Zonal distribution	134
Runoff zone	T403	Cluster distribution, free-form distribution	95	S65	Small-cluster distribution or free-form distribution	88
	T403	Cluster distribution, free-form distribution	95	S65	Small-cluster distribution or free-form distribution	88

(Continued on the following page)

10.3389/feart.2024.1395384

TABLE 2 (*Continued*) Thand distribution characteristics of inclusions in different zones.

Zone	Well	Distribution characteristic	Th (°C)	Well	Distribution Characteristic	Th (°C)
	T403	Cluster distribution, free-form distribution	98	S65	Small-cluster distribution or free-form distribution	89
	T403	Cluster distribution, free-form distribution	99	S65	Small-cluster distribution or free-form distribution	89
	T403	Cluster distribution, free-form distribution	99	S65	Small-cluster distribution or free-form distribution	90
	T403	Cluster distribution, free-form distribution	102	S65	Small-cluster distribution or free-form distribution	90
	T403	Cluster distribution, free-form distribution	102	S65	Small-cluster distribution or free-form distribution	90
	T403	Cluster distribution, free-form distribution	102	S65	Small-cluster distribution or free-form distribution	90
	T403	Cluster distribution, free-form distribution	102	S65	Small-cluster distribution or free-form distribution	90
	T403	Cluster distribution, free-form distribution	105	S65	Small-cluster distribution or free-form distribution	90
	T403	Cluster distribution, free-form distribution	105	S65	Small-cluster distribution or free-form distribution	90
	T403	Cluster distribution, free-form distribution	110	S65	Small-cluster distribution or free-form distribution	90
	T403	Cluster distribution, free-form distribution	110	S65	Small-cluster distribution or free-form distribution	90
	T403	Cluster distribution, free-form distribution	130	S65	Small-cluster distribution or free-form distribution	90
	T403	Cluster distribution, free-form distribution	130	S65	Small-cluster distribution or free-form distribution	90

(Continued on the following page)

TABLE 2 (*Continued*) Thand distribution characteristics of inclusions in different zones.

Zone	Well	Distribution characteristic	Th (°C)	Well	Distribution Characteristic	Th (°C)
	T403	Cluster distribution, free-form distribution	130	S65	Small-cluster distribution or free-form distribution	90
	T403	Cluster distribution, free-form distribution	135	S65	Small-cluster distribution or free-form distribution	90
	T403	Cluster distribution, free-form distribution	135	S65	Small-cluster distribution or free-form distribution	90
	T403	Cluster distribution, free-form distribution	135	S65	Small-cluster distribution or free-form distribution	90
	T403	Cluster distribution, free-form distribution	135	S65	Small-cluster distribution or free-form distribution	92
	T403	Cluster distribution, free-form distribution	135	S65	Small-cluster distribution or free-form distribution	92
	T403	Cluster distribution, free-form distribution	140	S65	Small-cluster distribution or free-form distribution	92
	T403	Cluster distribution, free-form distribution	140	S65	Small-cluster distribution or free-form distribution	92
	T403	Cluster distribution, free-form distribution	145	S65	Small-cluster distribution or free-form distribution	92
	T403	Cluster distribution, free-form distribution	145	S65	Small-cluster distribution or free-form distribution	92
	T403	Cluster distribution, free-form distribution	145	S65	Small-cluster distribution or free-form distribution	92
	T403	Cluster distribution, free-form distribution	145	S65	Small-cluster distribution or free-form distribution	92
	T403	Cluster distribution, free-form distribution	146	S65	Small-cluster distribution or free-form distribution	92

(Continued on the following page)

TABLE 2 (*Continued*) Thand distribution characteristics of inclusions in different zones.

Zone	Well	Distribution characteristic	Th (°C)	Well	Distribution Characteristic	Th (°C)
	T403	Cluster distribution, free-form distribution	146	S65	Small-cluster distribution or free-form distribution	93
	T403	Cluster distribution, free-form distribution	148	S65	Small-cluster distribution or free-form distribution	95
	T403	Cluster distribution, free-form distribution	148	S65	Small-cluster distribution or free-form distribution	95
	T403	Cluster distribution, free-form distribution	150	S65	Small-cluster distribution or free-form distribution	95
	T403	Cluster distribution, free-form distribution	150	S65	Small-cluster distribution or free-form distribution	95
	T403	Cluster distribution, free-form distribution	150	S65	Small-cluster distribution or free-form distribution	120
	T403	Cluster distribution, free-form distribution	153	S65	Small-cluster distribution or free-form distribution	120
	T403	Cluster distribution, free-form distribution	155	S65	Small-cluster distribution or free-form distribution	120
	T403	Cluster distribution, free-form distribution	155	S65	Small-cluster distribution or free-form distribution	120
	S65	Free-form distribution or small-cluster distribution	80	S65	Small-cluster distribution or free-form distribution	120
	S65	Free-form distribution or small-cluster distribution	80	S65	Small-cluster distribution or free-form distribution	124
	S65	Free-form distribution or small-cluster distribution	80	S65	Small-cluster distribution or free-form distribution	125
	S65	Free-form distribution or small-cluster distribution	80	S65	Small-cluster distribution or free-form distribution	125

(Continued on the following page)

10.3389/feart.2024.1395384

TABLE 2 (*Continued*) Thand distribution characteristics of inclusions in different zones.

Zone	Well	Distribution characteristic	Th (°C)	Well	Distribution Characteristic	Th (°C)
	S65	Free-form distribution or small-cluster distribution	80	S65	Small-cluster distribution or free-form distribution	128
	S65	Free-form distribution or small-cluster distribution	85	S65	Small-cluster distribution or free-form distribution	130
	S65	Free-form distribution or small-cluster distribution	85	S65	Small-cluster distribution or free-form distribution	130
	S65	Free-form distribution or small-cluster distribution	85	S65	Small-cluster distribution or free-form distribution	135
	S65	Free-form distribution or small-cluster distribution	85	S65	Small-cluster distribution or free-form distribution	135
	S65	Free-form distribution or small-cluster distribution	87	S65	Small-cluster distribution or free-form distribution	140
	S65	Small-cluster distribution or free-form distribution	88	S65	Small-cluster distribution or free-form distribution	140
	S65	Small-cluster distribution or free-form distribution	88	—	—	—
Discharge zone	T615	Cluster distribution	88	T615	Zonal distribution	85
	T615	Cluster distribution	90	T615	Zonal distribution	87
	T615	Cluster distribution	97	T615	Zonal distribution	93
	T615	Cluster distribution	102	T615	Zonal distribution	94
	T615	Cluster distribution	104	T615	Zonal distribution	98
	T615	Zonal distribution	80	T615	Zonal distribution	98
	T615	Zonal distribution	82	T615	Zonal distribution	101
	T615	Zonal distribution	82	T615	Zonal distribution	107

important stages of collapse–filling (Figure 9B). However, there are still other temperatures distributed on either side of the peaks that represent at least three or more stages of filling, and have a coinciding association with various types of inclusion forms. Well S65 is also an important well in the recharge area, where inclusion distribution is dominated by free-form and small-cluster inclusions, with the most significant peak (85°C–100°C) consistent with well T417.

Well T403 is located in the runoff area. The fluid inclusions in the well are mainly distributed in the cluster and free-form styles, and the homogenization temperature of the fluid inclusions shows two peaks, i.e., 100°C–115°C and 130°C–145°C, indicating

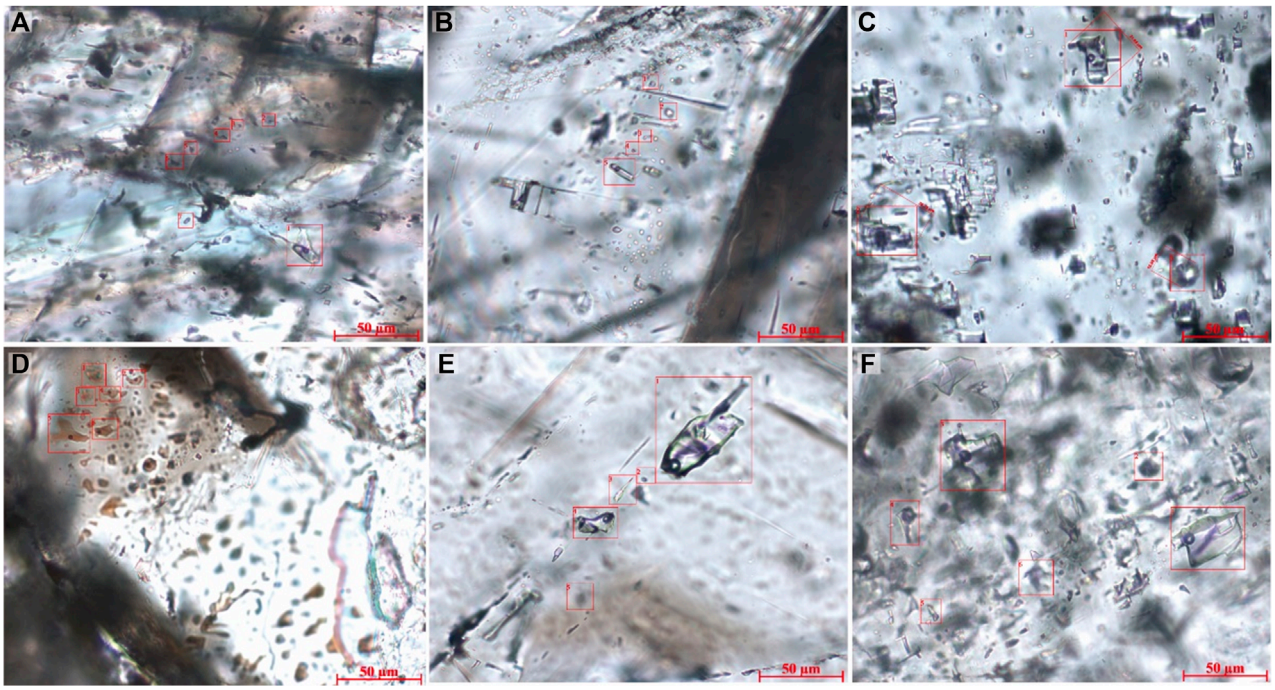

FIGURE 8
Micro-photographs of fluid inclusions from cores in the Tahe oilfield. **(A)** T417-4-6/29, 5507 m, calcite filled in dissolution fracture, zonal distribution along the healing fractures of calcite minerals; **(B)** T417-6-24/55,5563.3 m, calcite filled in fracture, zonal distribution along the healing fractures of calcite minerals; **(C)** T615-8-4/33, 5521.6 m, calcite filled in the karst cave, clustered distribution in calcite minerals; **(D)** T615-8-4/33, 5521.6 m, calcite filled in the karst cave, clustered distribution in calcite minerals; **(E)** T615-6-26/40, 5564 m, calcite filled in fracture, zonal distribution along the healing fractures of calcite minerals, T615-6-26/40, 5564.0 m. **(F)** T615-6-26/40, 5564.53 m, calcite filled in fracture, clustered distribution along the in calcite minerals.

at least two stages of collapse and filling process in the cave (Figure 9C). However, compared with samples from the recharge area, the peak value of homogenization temperature here is relatively higher, indicating that the filling period of the inclusions is lagging behind that of the recharge area. In addition, the maximum peak of homogenization temperature in the runoff area is 130°C–145°C, suggesting the filling period of the stronger filling in the runoff area may be later in terms of geological history. It can be seen from the morphology and distribution characteristics of inclusions in the runoff area that most of the inclusions were formed under the conditions of slow flow alternations and relatively stable change of solution concentration and had the environmental characteristics of buried paleo-karstification, which was the main reason for the occurrence of high-temperature inclusions in the area and also reflected that the main body filling period was late (Xia and Tang, 2004).

In the discharge zone, the fluid inclusions observed in well T615 are mainly distributed in clusters and zonations. Although a few samples were tested in this area compared with the other zones, the peak values of the homogenization temperature, between 85°C and 100°C, are in good agreement with both the recharge area and the runoff area (Figure 9E), indicating that the whole karst system underwent a relatively uniform collapse–filling process at the same stage as the recharge and runoff areas, that is, a contemporaneous or early diagenetic rock environment. The fluid at this stage is atmospheric fresh water, the homogenization temperature of fluid inclusions in calcite of this origin is low, and the oxygen isotope is more negative. However, in the discharge zone, there were large quantities of fillings observed with large volume differences and a certain cycle rhythm, which showed that there are hydrodynamic conditions at different stages and degrees, and there are also strong hydrodynamic conditions. This could be the reason why fewer inclusion samples were captured (Xia and Tang, 2004). In addition, Chen et al. (2023) also pointed out that multi-stage collapse filling existed in well T615, especially in the developmental burial stage.

The carbon–oxygen isotope results indicate that there were at least four stages of filling that could be observed in this area, of which the first stage (I in Figure 7) indicated the contemporaneous or early diagenetic rock environment. All samples from the three wells in the recharge–runoff–discharge zones confirmed that contemporaneous filling was generally developed in the three zones. The second stage samples (II in Figure 7) suggest an early-buried karst environment, which is supported by two data points from the recharge and discharge zones. Due to the small number of samples, it cannot be excluded that the runoff area also developed the same filling process at the same time, and this stage may also be the second filling process that generally develops. A late-buried karst environment dominated in the third stage (III in Figure 7), and only well samples in the runoff and recharge areas supported this stage, proving that filling began to migrate to the lower part of the runoff. During the fourth stage (IV in Figure 7), only well samples in recharge zones supported a

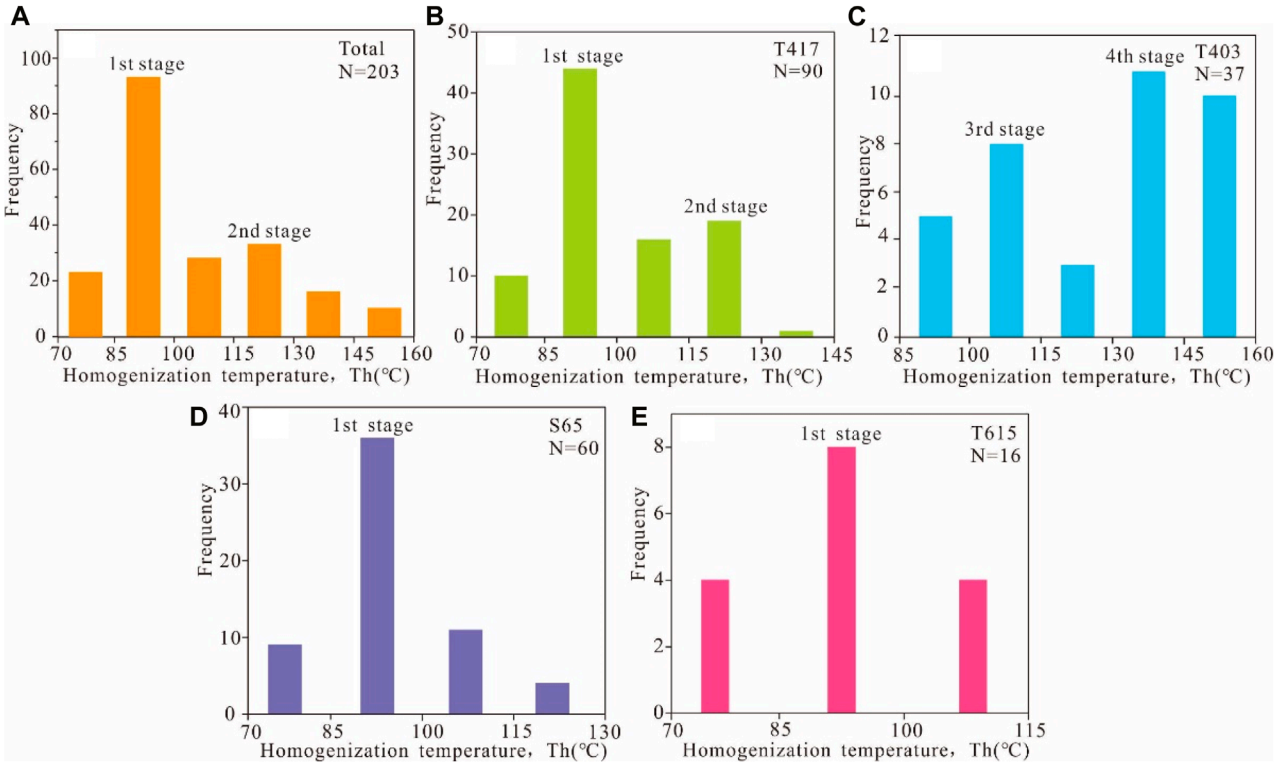

FIGURE 9
Diagram showing the frequency of homogenization temperature in recharge–runoff–discharge zones in the Tahe oilfield. **(A)** Total sample of four wells; **(B)** 90 samples in well T417; **(C)** 37 samples in well T403; **(D)** 60 samples in well S65; **(E)** 16 samples in well T615.

deep-buried environment, suggesting the basic law of filling process migration from the recharge area to runoff and the recharge area to a certain extent.

5.1.3 Collapse–filling stages and evolution in different recharge–runoff–discharge zones

On the basis of the above analysis, the paleo-underground river channels were proven to have experienced at least three stages of the collapse–filling process, which is supported by the filling characteristics of karst caves in the core, inclusion characteristics, and carbon–oxygen isotope results. The collapse–filling process shows obvious differences in the recharge, runoff, and recharge zones (Figure 10). In other words, the paleo-underground river channel system underwent multiple stages of the collapse–filling process, among which collapse–filling in different karst zones follows the evolution law of inheritance, development, and migration.

Although the collapse–filling stages are divided according to the characteristics of the core, fluid inclusions, and carbon–oxygen isotopes, the stages divided by different schemes are different. The stages divided according to the geochemical scheme are relatively simple and can be detected when the geological environment changes significantly. It cannot be excluded that the multiple filling processes occurred in a relatively stable karst environment in a short period of time. In addition, the matching relationship between geochemical analysis results and geological historical stages is relatively rough and limited by samples; therefore, some stages may not be fully detected. According to the stage division of core filling characteristics, the formation stage can be easily determined by changes in lithology and lithofacies, but the filling caused by changes in the karst environment is difficult to accurately identify by cores. It is relatively scientific to comprehensively analyze the change in the collapse–filling environment using the geochemical analysis method and the architectural change in the collapse–filling from cores to determine the stage. In addition, discussing the filling characteristics from different zones provides more effective evidence support for comparing the differences and migration patterns in recharge, runoff, and discharge zones.

Based on core observation and geochemical analysis, it is concluded that at least four stages of the collapse-filling process occurred in the study area. In the first stage of the underground river collapse–filling, a mixture of collapsed breccia and sandy mud was formed uniformly at the bottom of the cave (Figure 5), and similar values of the carbon–oxygen isotope in the three wells support this and have the characteristics of a large negative degree of oxygen isotope, suggesting a relatively uniformed syngenetic or early diagenetic rock environment (Figure 6). Jin et al. (2015) also obtained carbon and oxygen isotope values belonging to this stage from cave calcite. The relatively uniform first peak (85°C–100°C) of the homogenization temperature may be a response to the first stage. The first peak of fluid inclusion homogenization temperature (85°C–100°C) reflects the first filling stage, which

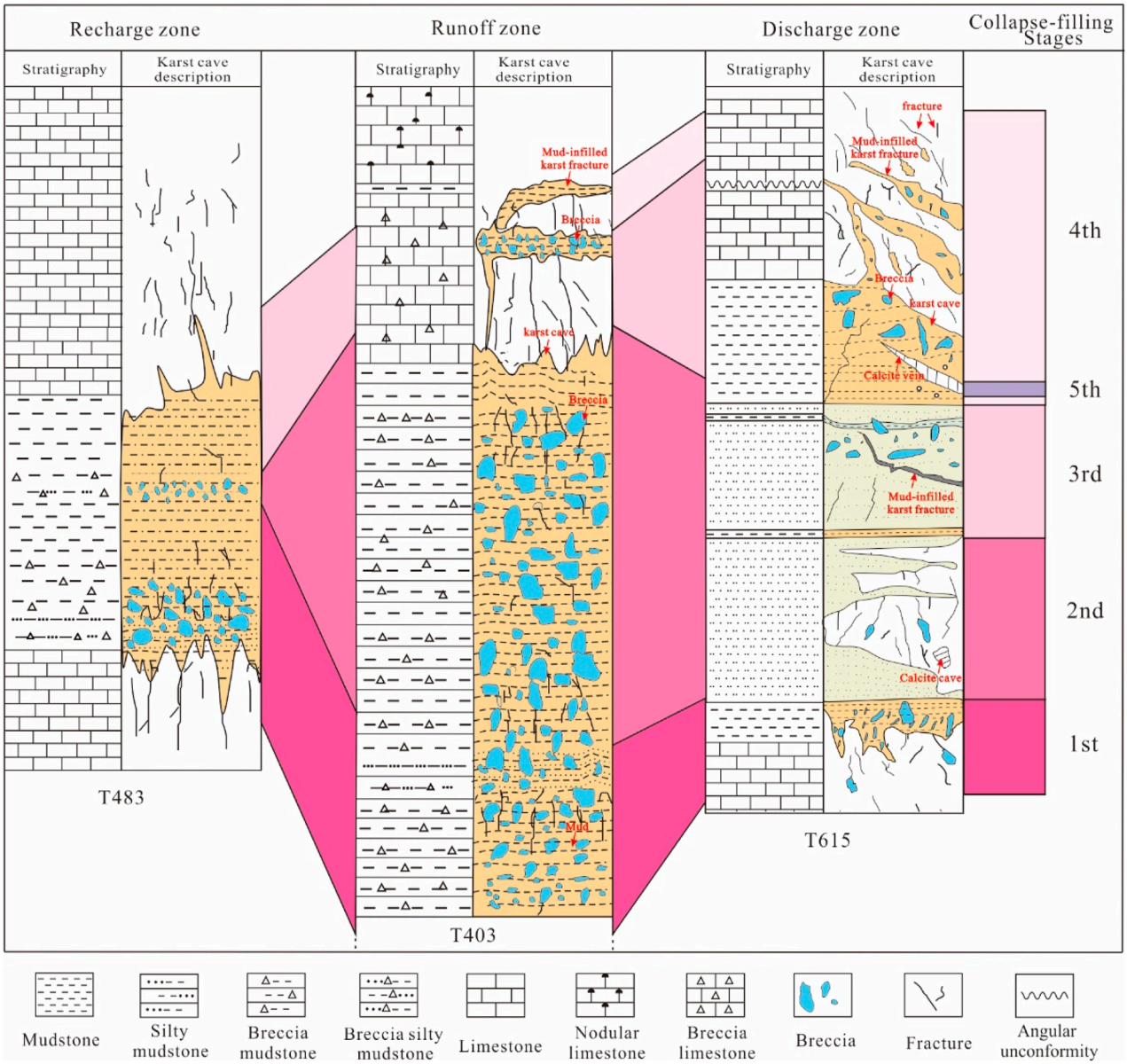

FIGURE 10
Comparison of differential collapse–filling stages in typical single wells in recharge–runoff–discharge zones (well locations are shown in Figure 3).

is consistent with the filling stage indicated by carbon and oxygen isotopes.

The mixed fillings, including karst breccia and mud, all exist at the bottom of the single hole in the three wells in the recharge, runoff, and discharge zones. Similar filling characteristics probably formed in the first uniform stage. Some caves in the core were observed to be filled with sand. All of the fillings were formed by the combination of karst collapse and the sand–mud filling carried by the runoff during the runoff process of the paleo-underground river and belong to the first-stage fillings of the underground river. The S80 well that Jin et al. (2015) dissected had similar characteristics. By using the U–Pb dating of calcite, Wei et al. (2023) obtained the age of ~466 Ma, which basically represents the environment of the early diagenzoic stage and has a time matching with the underground river filling in the first stage. However, the filling characteristics differ in the recharge, runoff, and discharge zones. The karst breccia in the recharge area is larger, gradually decreases in the runoff zone, and is smaller and more dispersed in the discharge area, which suggests that the main body of filling is mainly concentrated in the recharge area, and the filling material and collapse effect became weaker and weaker from the recharge to the runoff zone and the distal discharge zone.

A relatively unified karst breccia and sand-argillic mixed filling existed in the second stage of the paleo-underground river, which is supported by the relatively consistent karst breccia observed in three wells. The carbon–oxygen isotope data indicated an early buried karst environment, and the second peak of fluid inclusion

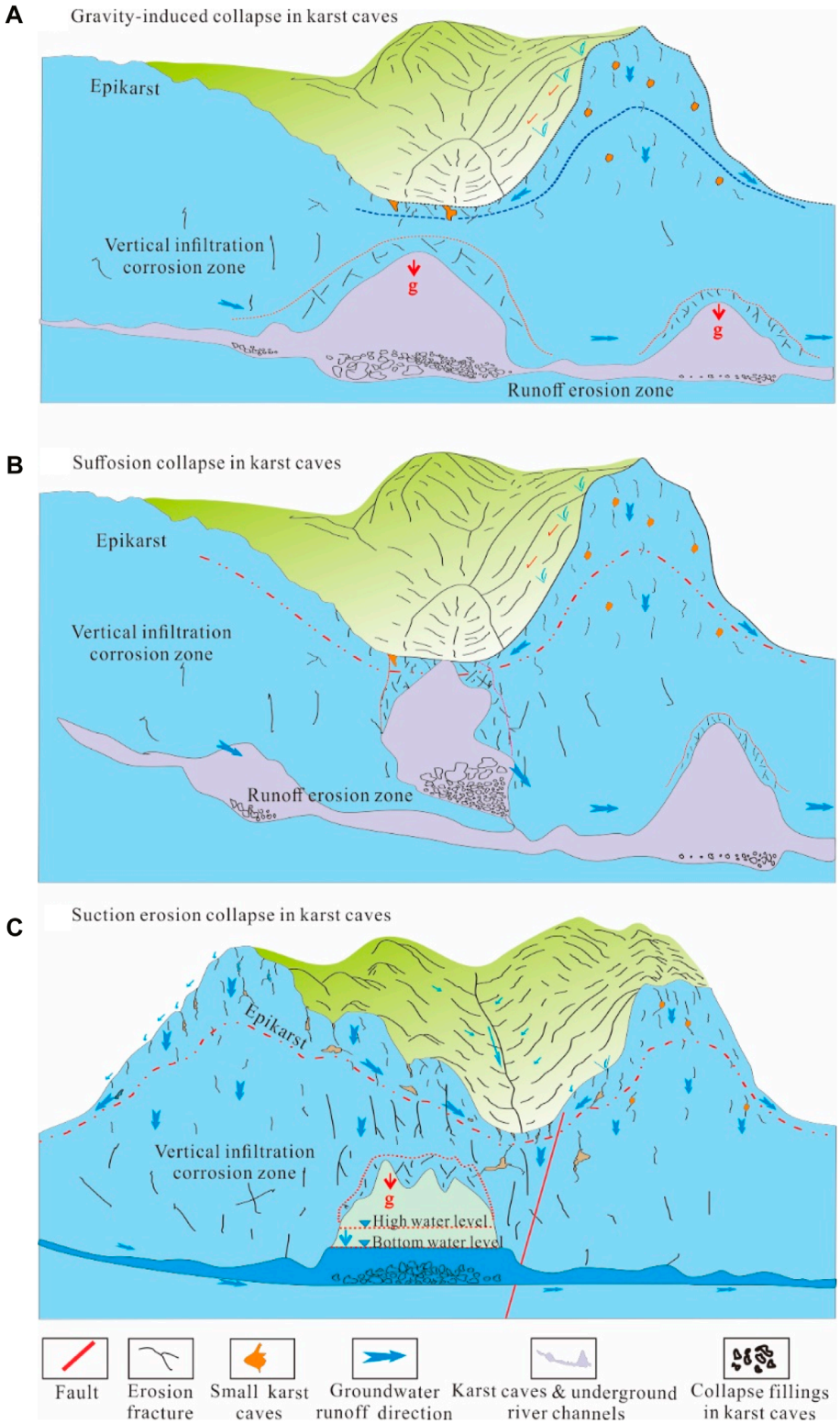

FIGURE 11
Different models illustrating different collapse–filling mechanisms in the Tahe oilfield. **(A)** model of gravity-induced collapse in karst caves; **(B)** model of suffosion collapse in karst caves; **(C)** model of suction erosion collapse in karst caves.

homogenization temperature (115°C–130°C) may be the response of this stage. However, filling differences also existed among the recharge, runoff, and discharge zones. Karst breccias decrease from the bottom to the middle part of the cave, while the opposite characteristics exist in the runoff zone, suggesting that the hydraulic power was relatively weakened in the recharge area and relatively

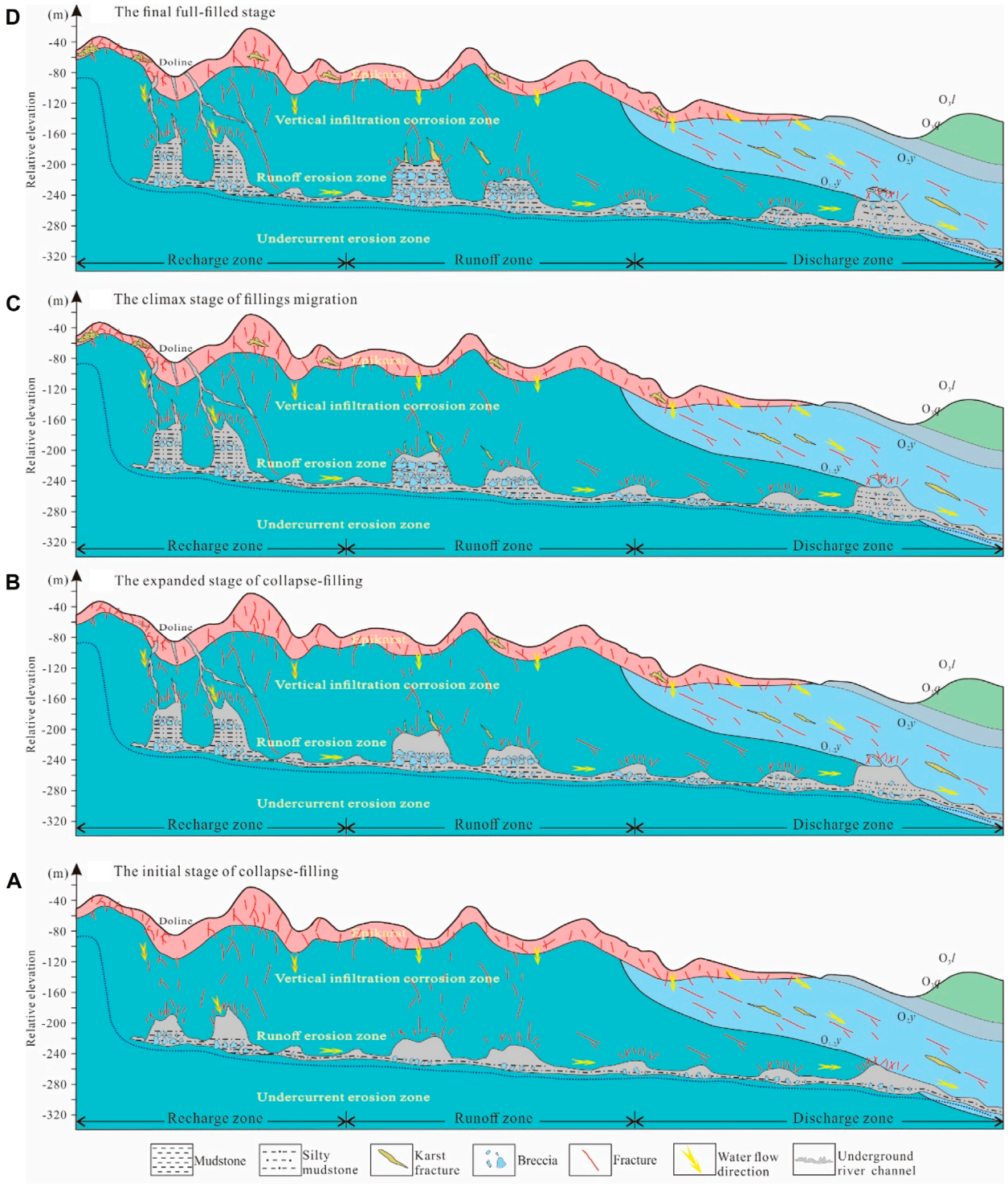

FIGURE 12
Collapse and filling evolution model of the paleo-underground river during different stages. **(A)** the initial stage of collapse-filling; **(B)** The expanded stage of collapse-filling; **(C)** The climax stage of fillings migration; **(D)** The final full-filled stage.

strengthened in the runoff area, that is, the main body of the filling was transferred from the recharge zone to the runoff zone. In addition, the migration of the peak homogenization temperature also suggests that the strong filling stage in the runoff area is slightly later than that of the recharge area, which is consistent with the above analysis.

The third-stage filling was formed in a deep burial environment, and the position of the third-stage carbon–oxygen isotopes indicated

that collapse–filling processes were mainly developed in runoff and discharge zones. Unlike the formation of relatively uniform collapse breccia and sand-argillaceous mixed sediments in the first and second stages, the paleo-underground river in the third stage may be filled with mud in the fractures in the top of the cave by vertical percolation in the recharge area, accompanied by collapse and sand-argillaceous filling of the top of the cave in the runoff and discharge zones.

The fourth-stage fillings were deposited in a deep-buried karst environment, and samples of carbon–oxygen isotopes indicated that fillings only existed in the discharge zone. The filling characteristics in the three zones were extremely inconsistent. In the discharge area, cave collapse and sand-argillaceous fillings could still be developed, and in the runoff area, mud filled in the fractures of the top of the cave; in the recharge area, fluid activities in the fractures dominated, and large-scale fillings were no longer developed. In the third and fourth stages, it is not excluded that small- and medium-scale fluid activities deposited in fractures and captured the fluid inclusions, and the inclusions with high homogenization temperatures probably formed in the recharge and runoff zones (Jin et al., 2015).

5.2 Mechanism change during the collapse–filling evolution process of the paleo-underground river

5.2.1 Collapse–filling styles of the paleo-underground river

The collapse of the karst cave is closely related to the scale, style, and structural condition of the surrounding rocks. Combining modern karst theory with core fill lithology and filling style, it is concluded that there are three important ways of collapse in the karst cave within the paleo-underground river in the Tahe area.

The first type is gravity-induced collapse (Figure 11A), which refers to the collapse process or phenomenon caused by the structural fractures of the surrounding rock and the gravity effect caused by its gravity on the top of a karst fracture-cave system, resulting in peeling layer by layer or overall collapse. Gravity-induced collapse is one of the most important modes of karst fracture caves, such as funnels (sinkholes), shafts, and other fracture caves located in depressions, which are often formed by this gravity-induced collapse.

The second type is suffusion-induced collapse (Figure 11B), which refers to the process and phenomenon of mechanical suffusion in the surrounding rocks of the karst fracture-cave system, which causes the surrounding rocks to be damaged and collapse when the hydraulic gradient is large enough under the action of groundwater seepage. This kind of collapse mode is generally located in karst fractures and caves in strong runoff zones and is a common collapse mode of karst caves in karst depressions, valleys, and low-lying areas of karst plain. This kind of collapse is not only affected by seepage but also affected by load loss and the gravity effect of the surrounding rocks.

The third type is suction-induced collapse (Figure 11C), which refers to the process and phenomenon of collapse caused by the failure of surrounding rocks when the negative pressure state is formed in the karst fracture and cave system with good sealing. This kind of collapse is affected not only by the absorption effect but also by the structural fractures and the gravity effect of the surrounding rocks.

5.2.2 Collapse–filling mechanism evolution of the paleo-underground river

Based on the collapse–filling characteristics of the karst cave, formation stages, and evolution processes of the paleo-underground river channel from the comprehensive analysis of core observation and geochemical data in the Tahe area, the study examined the styles and architectures of collapse–filling migration from the proximal recharge zone to the distal discharge zone during the evolution process. Therefore, the collapse–filling mechanisms probably changed during the different evolution stages.

In the early diagenetic environment or syngenetic stage of the karst evolution stage (Figure 12A), a unified mixed filling of karst breccia and calcareous clay was formed in the three zones, which is supported in the core observation in three wells of three zones. Meanwhile, the breccia was sharp-edged, and the breccia is more inclined to breccia deposition by collapse, which is the filling product formed in the early stage of karst caves formation and expansion. Due to the continuous runoff and groundwater percolation corrosion of underground rivers, the scale of karst caves gradually increases. In addition to the sand and mud carried by runoff and the residual breccia of karst caves, the cave filling is also filled by collapse breccia and the subsequent post-burial calcareous sediments. During this stage, the collapse and filling mechanism is mainly gravity-induced collapse with weak hydrodynamic force and other mechanisms in local areas.

In the early buried karst stage (Figure 12B), i.e., the second larger stage of collapse–filling, the recharge area (e.g., TK483) is still dominated by the mixed filling of the karst breccia and calcareous mud. The runoff area (e.g., T403) is characterized by a large amount of breccia, calcareous clay, and a small amount of sandy fill, and very thick sandy and shale fillings that existed in the discharge area (e.g., T615). These different phenomena suggest that the collapse–filling mechanism differs among the three zones. The mechanism in the recharge area is still dominated by gravity-induced collapse. A small amount of sand in the runoff area suggests a slightly enhanced hydrodynamic force, further indicating that the collapse–filling was primarily gravity-induced and local suffusion-induced mechanisms. A large amount of sand and mud filling in the discharge area confirms a strong hydrodynamic condition, and the suffusion-induced collapse–filling mechanism dominates, while the gravity-induced and suction-induced mechanisms locally influence the collapse–filling process.

In the climax filling karst stage (Figure 12C), the recharge area is dominated by calcareous filling, which is influenced by percolation; in the runoff area, the mixed filling of karst breccia and calcareous filling is dominated by gravity-induced collapse; in the discharge area, the strong hydraulic power carries the sandy and calcareous filling combined with karst breccia, which is controlled by the suffusion-induced mechanism or suction–erosion mechanism, and the gravity-induced action is also involved.

In the deep-buried karst stage (Figure 12D), only local fluid activity influenced by seepage is developed in the recharge zone

and runoff zone. In the discharge area, there is a mixed filling of karst breccia and calcareous mud, which is the product of a gravity-induced mechanism.

Therefore, the collapse mechanism of the paleo-underground river varies temporally and spatially along with the collapse–filling evolution process of the paleo-underground river, which confirms the transferability of the evolution of collapse mechanisms. The gravity-induced mechanism plays a long and wide leading role in the early collapse–filling stage of the paleo-underground river, as well as in the collapse–filling–shrinkage stages in the three zones. In the filling expanded and mature stages of the paleo-underground river, the suffusion-induced mechanism mainly influences the filling architecture in the runoff and discharge zones but is locally influenced by the gravity-induced mechanism.

6 Conclusion

Integration of core, fluid inclusion, and carbon–oxygen isotopic data from the Tahe area leads to the following conclusions:

(1) The paleo-underground river channel underwent a four-stage differential collapse–filling process in different recharge–runoff–discharge zones. The first collapse–filling stage was characterized by filling with breccia and calcium–mud material developed at the bottom of karst caves in the whole karst system. The widespread filling consisting of breccia and calcium–mud material was the main feature in the second stage, and local sand materials were infilled in the runoff zone and discharge zone. In the third stage, fewer fillings, breccia, calcium–mud material fillings, and sand materials were the main fillings in the recharge zone, runoff zone, and discharge zones, respectively. In the fourth stage, breccia and calcium–mud materials were only infilled in the discharge zone.

(2) Hydrodynamic strength and filling capacity vary spatiotemporally in the recharge zone, runoff zone, and discharge zone during the collapse–filling process. The hydrodynamic force and filling capacity dominate in the recharge zone during the initial stage, migrate to the runoff zone during the later stage, and concentrate in the discharge zone in the last stage.

(3) The collapse–filling mechanism varies along with the collapse–filling evolution process of the paleo-underground river. The gravity-induced mechanism dominates in the initial and late stages of the whole paleo-underground river system and dominates all the time in the recharge zone. The suffusion-induced mechanism dominates in the mature stage in runoff and discharge zones, while the suction–erosion mechanism is locally involved.

Data availability statement

The original contributions presented in the study are included in the article/Supplementary Material; further inquiries can be directed to the corresponding author.

Author contributions

H-QD: data curation, methodology, writing–original draft, and writing–review and editing. J-PL: data curation and writing–review and editing. Q-YZ: Data curation, Writing–original draft. J-RL: Methodology and Writing–review and editing. J-WW: Methodology, Writing–review and editing. G-QN: Data curation and Writing–original draft. Y-LL: Resources, Writing–original draft.

Funding

The author(s) declare that financial support was received for the research, authorship, and/or publication of this article. This research was funded by the Basic Research Funds of the Chinese Academy of Geological Sciences (JKYQN202367), the Guangxi Key Research and Development Plan Project (AB23026062), and the China Geological Survey Project (DD20221658).

Acknowledgments

The authors thank the editor, Xixin Wang, and two professional reviewers for their constructive comments and efforts. They appreciate Northwest Oilfield Branch of SINOPEC for data support. They thank Lujuan Li for data and graphics preparation and disposal.

Conflict of interest

The authors declare that the research was conducted in the absence of any commercial or financial relationships that could be construed as a potential conflict of interest.

Publisher's note

References

Ainsaar, L., Kaljo, D., Martma, T., Meidla, T., Männik, P., Nõlvak, J., et al. (2010). Middle and upper Ordovician carbon isotope chemostratigraphy in Baltoscandia: acorrelation standard and clues to environmental history. *Palaeogeogr. Palaeoclimatol. Palaeoecol.* 294 (3), 189–201. doi:10.1016/j.palaeo.2010.01.003

Bögli, A. (1980). *Karst hydrology and physical speleology*. Berlin: Springer-Verlag.

Cai, C. F., Li, K. K., and Li, B. (2009). Geochemical characteristics and origins of fracture-and vug-fillings of the Ordovician in Tahe oilfield,Tarim basin. *Acta Petrol. Sin.* 25 (10), 2399–2404.

Chen, H. H., Wu, Y., and Zhu, H. T. (2016). Eogenetic karstification and reservoir formation model of the Middle-Lower Ordovician in the northeast slope of Tazhong Uplift (in Chinese with English abstract), Tarim Basin. *Acta pet. sin.* 37, 1231–1246.

Chen, R. K. (1994). Application of stable oxygen and carbon isotope in the research of carbonate disgenetic environment. *Acta Sedimentol. Sin.* 4, 11–21.

Chen, X., Liu, W. H., and Bao, D. (2023). Ordovician palaeokarst caves in the Tahe oilfield:Burial age of cave fills and its implication for hydrocarbon reservoirs. *Earth Sci. Front.* 30 (4), 65–66. doi:10.12336/biomatertransl.2023.02.002

Dan, G. J., Zhou, C. G., and Liu, Y. H. (2023). Seismic characteristics of the paleo-underground river system in Ordovician carbonate paleo-buried hills in the western Lungu area. *Geophys. Geochem. Explor.* 47 (2), 290–299. doi:10.11720/wtyht.2023.1052

Dan, Y., Liang, B., and Cao, J. W. (2012). Geochemical features and environmental signifcances of deposits in Ordovician karstic fractures and caves, Lunnan area, Tarim Basin. *Petrol Geol. Exp.* 34 (6), 623–628.

Ford, D. C., and Williams, P. W. (1989). *Karst geomorphology and hydrology*. London: Unwin Hyman.

Haeri-Ardakani, O., Al-Aasm, I. S., and Coniglio, M. (2013). Petrologic and geochemical attributes of fracture-related dolomitization in Ordovician carbonates and their spatial distribution in southwestern Ontario, Canada. *Mar. Petroleum Geol.* 43 (3), 409–422. doi:10.1016/j.marpetgeo.2012.12.006

Hu, W. G. (2022). Paleokarst fracture-vug types and their reconstruction in buried hill area,Tahe oilfield,Tarim Basin. *Oil Gas Geol.* 43 (1), 43–53. doi:10.11743/ogg20220104

Hu, X. Y., Quan, L. S., and Qi, D. S. (2014). Cavern filling characteristics of fracture-vuggy carbonate reservoir in Tahe oilfield. *Special Oil Gas Reservoirs* 21 (1), 18–21. doi:10.3969/j.issn.1006-6535.2014.01.004

James, N. P., and Choquette, P. W.(1988). *Paleokarst*. New York: Springer-Verlag.

Jia, C. Z. (1997). Tectonic Characteristics and Petroleum, Tarim Basin. China: Geological Publishing House, 29–261 (in Chinese).

Jin, Q., Kang, X., and Tian, F. (2015). Genesis of chemical fillings in fracture-caves in paleo-karst runoff zone in Ordovician and their distributions in Tahe oilfield, Tarim Basin. *Acta Pet. Sin.* 36 (7), 791–798. doi:10.7623/syxb201507003

Kang, X. (2014). Filling of the fracture-cavity space in ordovician karstreservoirs of the Tahe oilfield and its reservoirs petrophysics. Master Degree Thesis. China: China University of Petroleum EastChina.

Kang, Z. H., Lu, X. B., and Tang, X. R. (2014). Recognition and seismic reflection structure of ordovician paleocave collapse in Tahe oilfield. *Xinjiang Geol.* 32 (4), 540–545. doi:10.3969/j.issn.1000-8845.2014.04.025

Klimchouk, A., Auler, A. S., Bezerra, F. H. R., Cazarin, C. L., Balsamo, F., and Dublyansky, Y. (2016). Hypogenic origin, geologic controls and functional organization of a giant cave system in precambrian carbonates, Brazil. *Geomorphology* 253 (15), 385–405. doi:10.1016/j.geomorph.2015.11.002

Lauritzen, S. E., and Lundberg, J. (2000). "Solutional and erosional morphology of caves," in *Speleogenesis: evolution of karst aquifers*. Editors A. Klimchouk, A. Palmer, D. Ford, and W. Dreybrodt (Huntsville, Al: National Speleological Society), 408–426.

Li, K. P., Chen, H. H., and Feng, Y. (2012). Characteristics of homogenization temperatures of fluid inclusions and application in deeply buried carbonate rocks. *Nat. Gas. Geosci.* 23 (4), 756–763.

Li, P., Ren, J. Y., and Yang, H. Z. (2011). Hydrothermal activities in the fault system and their effects on carbonate rocks in the bachu area. *Geotect. Metallogenia* 35 (3), 378–385. doi:10.3969/j.issn.1001-1552.2011.03.007

Li, X. H., Kang, L. I. J., and Zhang, Y. W. (2021). Characteristics identification and formation of ordovician karst collapse reservoir structure in Tahe oilfield. *Geoscience* 35 (6), 1830–1843. doi:10.19657/j.geoscience.1000-8527.2021.187

Li, Z. H., Qiu, L. W., and Sun, B. Q. (2013). Characteristics of fluid inclusion and charging events of natural gas in Permian Jiamuhe Formation of Zhongguai area, Junggar Basin. *Nat. Gas. Geosci.* 24 (5), 931–939.

Liu, C. G., Li, G. R., and Zhang, Y. W. (2007). Application of strontium isotope to the study of paleokarst——an case from ordovician in the Tahe oilfield, Tarim Basin. *Acta Geol. Sin.* 81 (10), 1398–1406.

Liu, C. G., Zhang, Y., and Lu, H. T. (2008). Genesis and evolution of gigantic calcites in paleokarstic caves of middle-lower ordovician in Tahe oilfield. *Geol. Sci. Technol. Inf.* 27 (4), 33–38.

Liu, C. Y., Wu, M. B., and Gong, G. (2006). Caledonian karstification of Ordovician carbonates in the Tahe oilfield, northern Tarim basin, Northwest China, and its petroleum geological significance. *Geol. Bull. CHINA* 25 (9), 1128–1134. doi:10.3969/j.issn.1671-2552.2006.09.025

Liu, J. J., Mao, C., and Wei, H. H. (2021). Ordovician fracture-cavity filling sequence and its logging responses in Tahe Oilfield. *Xinjiang Pet. Geol.* 42 (1), 46–52. doi:10.7657/XJPG20210106

Liu, X. F., and Cai, Z. X. (2009). Element geochemistry characteristics of karstic cave deposit in Tahe Oilfield and its environmental significance. *Geol. Sci. Technol. Inf.* 28 (3), 53–57. doi:10.3969/j.issn.1000-7849.2009.03.009

Liu, X. F., Cai, Z. X., Yun, L., and Xu, W. (2009). Element geochemistry characteristic response for karstification in the Tahe Oilfield. *Petroleum Geol. Exp.* 31 (3), 270–274.

Loucks, R. G., Mescher, P. K., and Mcmechan, G. A. (2004). Three-dimensional architecture of a coalesced, collapsed-paleocave system in the Lower Ordovician Ellenburger Group, central Texas. *AAPG Bull.* 88 (5), 545–564. doi:10.1306/12220303072

Lyu, X., Wang, Y., and Yang, D. (2020). Characterization of paleo-karst reservoir and faulted karst reservoir in Tahe Oilfield, Tarim Basin, China. *Adv. Geo-Energy Res.* 4 (3), 339–348. doi:10.46690/ager.2020.03.11

Lyu, X. R., Wu, X. W., and Sun, J. F. (2022). Physical simulation and distribution prediction of karst cave collapsing in deep carbonate reservoirs. *Oil Gas Geol.* 43 (6), 1505–1514. doi:10.11743/ogg20220619

Meng, Q. Q., Zhu, D. Y., and Jie, Q. L. (2011). Controlling factors for deep fluid activity and prediction of positive effect area in middle Tarim and Bachu regions. *Petroleum Geol. Exp.* 33 (6), 597–601. doi:10.3969/j.issn.1001-6112.2011.06.008

Palmer, A. N. (2007). *Cave geology*. Dayton, Ohio: Cave Books.

Qi, L. X., and Yun, L. (2010). Development characteristics and main controlling factors of the Ordovician carbonate karst in Tahe oilfield. *Oil Gas Geol.* 31 (1), 1–12.

Qian, Y. X., Chen, Q. L., and Chen, Y. (2009). Mineralogical and geochemical identification for diagenetic settings of paleo-caves and fractures-filling and vugs calcites in carbonate:Taking wells S79 and S85 for example. *ACTA SEDIMENTOL. SIN.* 27 (6), 1027–1032.

Qian, Y. X., He, Z. L., and Zou, Y. R. (2008). The meteoric diagenesis of the Upper Ordovician carbonate rocks occurred insyn-sedimentary karstification in the No. 1 belt of Northwestern Tazhong, Tarim basin-taking the Well Shur-2 as an example. *Earth Sci. Front.* 15 (2), 59–66.

Qiang, J., Fei, T., and Xinbian, L. (2015). Characteristics of collapse breccias filling in caves of runoff zone in the Ordovician karst in Tahe oilfield,Tarim Basin. *Oil Gas Geol.* (5), 729–735. doi:10.11743/ogg20150503

Shi, S. Y., Hu, S. Y., and Liu, W. (2015). Distinguishing paleokarst period by integrating carbon-oxygen isotopes and fluid inclusion characteristics. *Nat. Gas. Geosci.* 26 (2), 208–217. doi:10.11764/j.issn.1672-1926.2015.02.0208

Sun, M. S., Liu, C. Y., and Yang, Y. (2017). The forward modeling of fracture and cave carbonate reservoirs of the Yingshan Formation in Tazhong area, Tarim Basin. *Earth Sci. Front.* 24 (5), 339–349. doi:10.13745/j.esf.yx.2016-11-48

Sun, S., Zhao, W. Z., Zhang, B. M., Liu, J., Zhang, J., and Shan, X. (2013). Observation and implication of the paleo-cave sediments in ordovician strata of well lun dong-1in the Tarim Basin. *Sci. China:Earth Sci.* 56 (4), 618–627. doi:10.1007/s11430-012-4563-4

Wang, B. Q., and Al-Aasm, I. S. (2002). Karst-controlled diagenesis and reservoir development: example from the Ordovician main reservoir carbonate rocks on the eastern margin of the Ordos Basin, China. *AAPG Bull.* 86 (9), 1639–1658. doi:10.1306/61eedd28-173e-11d7-8645000102c1865d

Wang, C., Zhang, Q., and Xiang, W. (2017). Physical and numerical modeling of the stability of deep caverns in Tahe oil field in China. *Energies* 10 (6), 769. doi:10.3390/en10060769

Wang, Y., Gao, J. Y., and Yang, D. B. 2023. Development conditions and geological models of large dendritic karst conduit in early Hercynian: a case study of B94 well block of Tahe Oilfield, Tarim Basin. Fault-Block Oil and Gas Field, 30(5): 758–769 .

Wei, D., Gao, Z. Q., Zhang, L. L., Fan, T., Wang, J., Zhang, C., et al. (2023). Application of blocky calcite vein LA-MC-ICP-MS U–Pb dating and geochemical analysis to the study of tectonic–fault–fluid evolutionary history of the Tabei Uplift, Tarim Basin. *Sediment. Geol.* 453, 106425. doi:10.1016/j.sedgeo.2023.106425

Winter, B. L., and Knauth, L. P. (1992). Stable isotope geochemistry of carbonate fracture fills in the Monterey Formation, California. *J. Sediment. Petrology* 62 (2), 208–219. doi:10.1306/d42678c5-2b26-11d7-8648000102c1865d

Wu, M., Zeng, C. B., and Huang, S. J. (2010). Fluid inclusion study of the Ordovician carbonate rock reservoir in the Tahe Oilfield. *Geol. China* 37 (5), 1360–1373.

Xia, R. Y., and Tang, J. S. (2004). Indication of mineral inclusion characteristics to palaeokarst actions. *Acta Geosci. Sin.* 25 (3), 373–377. doi:10.3321/j.issn:1006-3021.2004.03.017

Xia, R. Y., Tang, J. S., and Zou, S. Z. (2006). Features of the inclusion in paleo-karst fillings at the north edge of Tarim Basin. *Carsologica Sin.* 25 (3), 246–249. doi:10.3969/j.issn.1001-4810.2006.03.011

Xia, R. Y., Zou, S. Z., and Liang, B. (2011). *Fracture-cavity system model and its genetic research in the ordivician carbonate, Tarim Basin*. Beijing: Geological Publishing House.

Xu, J. H., Kang, Z. H., and Lan, Q. Q. (2020). Karst reservoir type, cave structure and genetic model of ordovician Tahe reservoirs:case study of fracture-cavity unit T615 in Tahe oilfield 7 block. *Geoscience* 3 (6), 1181–1192.

Xu, W., Cai, Z. X., and Jia, Z. Y. (2010). The study on ordovician carbonate reservoir karst cavern fillings characterization in Tahe oilfield. *Geoscience* 24 (2), 287–293. doi:10.3969/j.issn.1000-8527.2010.02.013

Xu, W., Cai, Z. X., and Lin, Z. M. (2012). Karst genesis classification of ordovician carbonate reservoir in Tahe oilfield, Tarim Basin. *Mar. Orig. Pet. Geol.* 17 (1), 66–72. doi:10.3969/j.issn.1672-9854.2012.01.010

Yu, H. F., Bai, Z. K., and Deng, L. P. (2011). Determination and geologic significance of Yingshan unconformity of lower Ordovician in Tazhong area, Tarim Basin (in Chinese with English abstract). *Xinjiang Pet. Geol.* 32, 231–234.

Yuan, D. X. (1993). *China Karstology*. Beijing: Geology Press, 4–8. (In Chinese).

Zhang, H. (2020). *Formation mechanism of middle-lower Ordovician karst reservoirs in Tarim Basin and the comparison with similar reservoirs in Permian Basin*. Wuhan: China University of Geosciences.

Zhang, H. T., Wang, J. Z., and Yang, M. (2020). Method research of quantitative evaluation on Ordovician carbonate reservoirs in western Tazhong area of Tarim Basin. *Xinjiang Oil Gas* 16 (1), 4–10. doi:10.3969/j.issn.1673-2677.2020.01.003

Zhang, H. T., Yang, M., and Wang, Y. (2021). Mechanical filling characteristics of Ordovician Karst paleo-subterranean rivers in Karst stage of Tahe oilfield. *Petroleum Geol. Eng.* 35 (6), 12–17. doi:10.3969/j.issn.1673-8217.2021.06.003

Zhang, J., Bao, D., and Yang, M. (2018). Analysis on fracture-cave structure characteristics and its controlling factor of paleo-subterranean rivers in the western Tahe Oilfield. *Petroleum Geol. Recovery Effic.* 25 (4), 33–39. doi:10.13673/j.cnki.cn37-1359/te.2018.04.006

Zhang, T., and Cai, X. Y. (2007). Caledonian paleo-karstification and its characteristics in Tahe area, Tarim Basin. *Acta Geol. Sin.* 81 (8), 1125–1134. doi:10.3321/j.issn:0001-5717.2007.08.012

Zhang, T., Yun, L., and Wu, X. W. (2005). The application of strontium isotopes in division of paleokarst stages in Tahe Oil Field. *Petroleum Geol. Exp.* 27 (3), 299–303. doi:10.3969/j.issn.1001-6112.2005.03.018

Zhang, W. B., Jin, Q., and Xu, S. Y. (2012). Filling characteristics of paleokarst cave in Ordovician outcrop in Tabei and its significance for oil and gas reservoir. *Special Oil Gas Reservoirs* 19 (3), 50–54. doi:10.3969/j.issn.1006-6535.2012.03.012

Zhang, X. L. (1985). Relationship between carbon and oxygen stable isotope in carbonate rocks and paleosalinity and paleotemperature of seawater. *Acta Sedimentol. Sin.* 3 (4), 17–30.

Zhang, Y., Peng, S. T., and Ji, S. Z. (2017). Filling degree prediction of ordovician paleocave and the application in yuqixi area of Tahe oilfield. *Xinjiang Geol.* 35 (1), 89–93. doi:10.3969/j.issn.1000-8845.2017.01.015

Zhang, Z. J., Lu, Y. P., and Ma, H. L. (2023). Fracture-cave system in collapsed underground paleo-river with subterranean flow in karst canyon area, Tahe Oilfield. *Xinjiang Pet. Geol.* 44 (1), 9–17. doi:10.7657/XJPG20230102

Zou, S. Z., Xia, R. Y., and Liu, L. (2016). Vertical zone characteristics and identification standard of Ordovician karst reservoirs in the Tahe Oilfield. *Acta Geol. Sin.* 90 (9), 2490–2501.